

The End Point of Nonaxisymmetric Black Hole Instabilities in Higher Dimensions

Hans Bantilan, Pau Figueras, Markus Kunesch,* and Rodrigo Panosso Macedo
*School of Mathematical Sciences, Queen Mary University of London,
Mile End Road, London E1 4NS, United Kingdom*

We report on the end state of non-axisymmetric instabilities of singly spinning asymptotically flat Myers Perry black holes. Starting from a singly-spinning black hole in $D = 5, 6, 7$ dimensions, we introduce perturbations with angular dependence described by $m = 2$ or $m = 4$ azimuthal mode numbers about the axis of rotation. In $D = 5$ we find that all singly spinning Myers-Perry black holes are stable, in agreement with the results from perturbation theory. In $D = 6$ and 7 , we find that these black holes are non-linearly stable only for sufficiently low spins. For intermediate spins, although the $m = 2$ bar mode becomes unstable and leads to large deformations, the black hole settles back down to another member of the Myers-Perry family via gravitational wave emission; surprisingly, we find that *all* such unstable black holes settle to the *same* member of the Myers-Perry family. The amount of energy radiated into gravitational waves can be very large, in some cases more than 80% of the initial total mass of the system. For high enough spins, the $m = 4$ mode becomes the dominant unstable mode, leading to deformed black holes that develop local Gregory-Laflamme instabilities, thus forming a naked singularity in finite time, which is further evidence for the violation of the weak cosmic censorship conjecture in asymptotically flat higher dimensional spacetimes.

I. INTRODUCTION

Black holes play a central role in general relativity (GR), the currently accepted classical theory of gravity. The recent direct detections of gravitational waves from black hole binary mergers [1] together with the image of the shadow of the black hole at the center of the M87 galaxy by the Event Horizon Telescope [2], have changed the perception of these objects from the purely mathematical to the “tangible”. All these observations are compatible with an equilibrium (or quasi-equilibrium) state that is described by the Kerr black hole [3]. However, the astrophysical relevance of the Kerr black hole hinges on whether it is non-linearly stable or not. All the evidence indicates that it is indeed stable, but a rigorous proof of the non-linear stability of the Kerr black hole is not yet available.

Following the discovery of the Gregory-Laflamme (GL) instability [4] of black strings and black branes in dimensions 5 and higher, black holes have become useful as laboratories to study dynamical instabilities, particularly due to their simplicity and their fundamental role in GR. The study of the evolution of black hole instabilities in the fully non-linear regime has been a fruitful area of research; indeed, the pioneering work of Lehner and Pretorius [5], with numerical simulations of the evolution of the GL instability of black strings in 5 dimensions, provided evidence that the weak cosmic censorship conjecture is false in asymptotically Kaluza-Klein spaces.

In higher dimensional asymptotically flat spaces, the situation is qualitatively similar. Black rings [6, 7] are asymptotically flat rotating black holes with horizon topology $S^1 \times S^n$. In the limit of large angular momentum along the S^1 , black rings resemble thin (boosted) black strings and hence they ought to be unstable under a GL type of instability. This was confirmed in Ref. [8]. Ref. [9] used numerical general relativity to simulate the non-linear evolution of black ring instabilities, and showed that thin enough black rings evolve into

naked singularities in finite time, thus potentially violating the weak cosmic censorship in higher dimensional asymptotically flat spaces.¹ This situation is not unique to black rings. In fact, a general picture of the stability/instability properties of higher dimensional black holes has emerged. Emparan and Myers [10] had noticed that rapidly rotating black holes in higher dimensions, i.e. Myers-Perry black holes (MP BHs), resemble black membranes and hence should also be GL unstable. Higher dimensional black holes generically admit a regime of large angular momentum with highly deformed horizons described by largely separated length scales, captured by the so-called blackfolds [11], that are expected to be dynamically unstable. To complete this general picture, it is thus important to determine the endpoint of these black hole instabilities in the rapidly spinning regime.

The instability of MP BHs was confirmed in [12] for linearized axisymmetric perturbations on top of an MP BH background.² A fully non-linear evolution of this axisymmetric instability of MP BHs revealed a sequence of concentric rings connected by black brane segments that became progressively thinner, eventually leading to a naked singularity in finite asymptotic time [14]. In the MP case, the dynamics of the horizon is not self-similar, unlike what was seen in the black string. The study of non-axisymmetric instabilities was initiated by Shibata and Yoshino in [15, 16]. For an MP BH in D dimensions with mass parameter μ and spin parameter a , these non-axisymmetric instabilities set in at smaller dimensionless spin $a/\mu^{1/(D-3)}$ than the axisymmetric instabilities.

Rotating black holes become dynamically unstable for values of $a/\mu^{1/(D-3)} \sim O(1)$. Indeed, from thermodynamic

¹ There are several issues that still need to be addressed, in particular, the structure of null infinity. In these dynamical spacetimes that develop naked singularities, it is not clear whether null infinity is incomplete.

² MP BHs with equal spins on all rotation planes are also known to be unstable [13]. For these black holes, unlike the singly spinning ones, the total angular momentum is bounded and hence the endpoints of their instabilities can potentially be quite different. We will not consider MP BHs with equal spins in this article.

* Until August 2018

considerations of the case where an MP BH fragments and expels two non-spinning BHs, Emparan and Myers [10] estimated that nonaxisymmetric instabilities should set in at around $a/\mu^{1/(D-3)} \approx 1$. Refs. [15, 16] found that MP BHs with $a/\mu^{1/(D-3)} \lesssim 0.7$ are stable in $D = 5, 6, 7$, but for higher spins the MP BHs are linearly unstable to a deformation whose azimuthal angle dependence is $e^{im\phi}$ for $m = 2$ i.e., a bar mode deformation. In 6 and 7 dimensions [16], they found that due to gravitational wave emission, this bar mode instability saturates and eventually damps, and the black hole settles down to an MP BH with a lower spin. A study of quasinormal modes of MP BHs [17] corroborates these results, except in the 5D case: whilst Ref. [15] found an instability, Ref. [17] did not find an exponentially growing mode in the linear regime. These two results could be compatible with each other if in 5D the instability were non-linear. In this article we resolve the apparent tension between these linear and the non-linear results. Analogous to the GL instability of black strings, for which higher harmonics become unstable for sufficiently thin strings, one would expect that for sufficiently large $a/\mu^{1/(D-3)}$, modes with $m > 2$ become the dominant unstable modes. This is indeed the case for black rings [9], and we show here that the same happens for MP BHs.

In this paper, we investigate the nonlinear evolution of MP BHs in $D = 5, 6, 7$ dimensions with dimensionless spins of $0.7 \leq a/\mu^{1/(D-3)} \leq 1.5$, and perturbed by nonaxisymmetric deformations described by the $m = 2$ and $m = 4$ azimuthal mode numbers. We use the cartoon method [16, 18, 19] to impose an $SO(D-3)$ symmetry that still captures the non-axisymmetric instability while allowing us to restrict to $3+1$ dynamics in D dimensions. We believe that this symmetry assumption should still be enough to capture the essential physics of the non-axisymmetric instabilities and their endpoints.

The rest of this article is organized as follows: in Section §II we provide an overview of the numerical methods that we used in our simulations. Section §III constitutes the bulk of the article, where we present our results for the non-linear evolution of unstable MP BHs in various spacetime dimensions and for different values of the dimensionless spin parameter. We summarize our results and conclude in Section §IV. Technical results are collected in the appendices. In Appendix §A we review the notion of asymptotic flatness in higher dimensions introduced in [20], and how the matrix of Weyl scalars captures gravitational radiation. In Appendix §B we collect several properties of tensor spherical harmonics. Appendices §C and §D contain the tensor harmonics on the S^3 and the S^4 respectively that we have used in our extractions. In Appendix §E we review the transformation properties of the multipoles of the Weyl tensor under changes of basis. In Appendix §F we compare the contours of χ with the apparent horizon and Appendix §G contains some convergence tests.

II. NUMERICAL METHODS

In this section we summarize the numerical methods that we have employed in our simulations. In subsection §II A we

describe our evolution scheme together with the our choice of initial data and gauge evolution equations. In section §II B we provide some details about our approach to extracting gravitational waves in higher dimensions.

A. Evolution scheme

The results presented here are obtained by solving the Einstein field equations in the CCZ4 formulation [21, 22]. We use Cartesian coordinates to solve for the evolution of asymptotically flat black hole solutions in $D = 5, 6, 7$ dimensions while imposing an $SO(D-3)$ symmetry using the modified cartoon method [16, 18, 19]. We redefine the constraint damping parameter $\kappa_1 \rightarrow \kappa_1/\alpha$ as in [23], where α is the lapse function, and we typically use constraint damping values $\kappa_1 = 0.4, \kappa_2 = 0$. As in [14], we use initial data for a singly spinning MP BH,

$$ds^2 = -dt^2 + \frac{\mu}{r^{D-5}\Sigma}(dt - a \sin^2 \theta d\phi)^2 + \frac{\Sigma}{\Delta} dr^2 + \Sigma d\theta^2 + (r^2 + a^2) \sin^2 \theta d\phi^2 + r^2 \cos^2 \theta d\Omega_{(D-4)}^2, \quad (1)$$

where $\Sigma = r^2 + a^2 \cos^2 \theta$, $\Delta = r^2 + a^2 - \mu r^{5-D}$, and μ and a are the mass and spin parameters of the MP BH. In analogy with the transformation from Schwarzschild coordinates to isotropic coordinates in D dimensions, we define a new radial coordinate ρ ,

$$r = \rho \left[1 + \frac{1}{4} \left(\frac{r_h}{\rho} \right)^{D-3} \right]^{\frac{2}{D-3}} \quad (2)$$

where r_h is the largest real root of $\Delta(r_h) = 0$. Then, the Cartesian coordinates are given by

$$\begin{aligned} x &= \rho \sin \theta \cos \phi, \\ y &= \rho \sin \theta \sin \phi, \\ z &= \rho \cos \theta \cos \varphi_1, \\ w_1 &= \rho \cos \theta \sin \varphi_1 \cos \varphi_2, \\ &\dots \\ w_{D-4} &= \rho \cos \theta \sin \varphi_1 \dots \sin \varphi_{D-3}. \end{aligned} \quad (3)$$

Imposing the $SO(D-3)$ symmetry corresponds to working on the slice $w_1 = \dots = w_{D-4} = 0$, see [16, 18, 19].

For values of $a/\mu^{1/3} \sim 1.5$, numerical noise is enough to trigger the instability in the $m = 4$ sector. Note that although the initial (rapid) gauge adjustment induces a small burst of radiation that in practice contains modes with different m , this initial burst is induced by truncation error and hence is under control and small. For smaller values of the dimensionless spin, we trigger the instability by hand through an $m = 2$ or $m = 4$ deformation of the conformal factor χ :

$$\chi = \chi_0 \left\{ 1 + A f_m(x, y) \times \exp \left[- \left(\frac{\operatorname{atanh}(\chi_0)}{\operatorname{atanh}(\chi_H)} - \frac{\operatorname{atanh}(\chi_H)}{\operatorname{atanh}(\chi_0)} \right)^2 \right] \right\}, \quad (4)$$

where χ_0 is the conformal factor computed from the analytic initial data (1), χ_H is some value of the conformal factor close to the apparent horizon, A is the amplitude of the perturbation and $f_m(x, y)$ is the function that induces the desired deformation:

$$\begin{aligned} m = 2 : \quad f_2(x, y) &= x^2 - y^2, \\ m = 4 : \quad f_4(x, y) &= x^4 - 6x^2y^2 + y^4. \end{aligned} \quad (5)$$

For some simulations, we also introduce this deformation in χ after the gauge adjustment period at around $t/\mu^{\frac{1}{D-3}} \sim 10$, but in practice doing this as opposed to introducing the deformation at $t/\mu^{\frac{1}{D-3}} = 0$ does not have a significant effect. This method of perturbing the black hole violates the constraints, so even though the CCZ4 formulation quickly³ takes us back to the constraint surface, we do not have control over where on the constraint surface we land. Therefore, to make sure that the mass and angular momentum of the perturbed data are not too far from those of the original MP BH we keep A small (a typical value that we use is $A = 0.02$).

We evolve the lapse with the standard 1 + log slicing condition [21],

$$(\partial_t - \beta^i \partial_i) \alpha = c_\alpha \alpha (K - 2\Theta), \quad (6)$$

where c_α is a freely adjustable coefficient. In our runs we found that $c_\alpha = 1.5$ worked well for $D = 5, 6, 7$.⁴ To evolve the shift, we used the modified Gamma-driver condition introduced in [9],

$$(\partial_t - \beta^j \partial_j) \beta^i = c_\beta \left(\hat{\Gamma}^i - f(t, \rho) \bar{\Gamma}^i \right) - \eta \beta^i, \quad (7)$$

where $\hat{\Gamma}^i$ is the usual CCZ4 evolution variable, $\bar{\Gamma}^i$ is the contracted Christoffel symbol computed from the (conformally rescaled) initial data (1), and

$$f(t, \rho) = \exp \left[- \left(\frac{t}{\mu^{1/(D-3)}} \right)^2 \left(\delta_1 \left(\frac{\rho_h}{\rho} \right)^2 + \delta_2 \right) \right], \quad (8)$$

with $\rho_h = r_h/(4^{\frac{1}{D-3}})$ and $\delta_{1,2}$ are two adjustable parameters that control the decay of the initial gamma function near the horizon. Since the initial data has $\bar{\Gamma}^i \neq 0$, the role of the extra term in (7) is to drive the gauge towards $\bar{\Gamma}^i = 0$ whilst making sure that the right hand side of the equation remains relatively small throughout the evolution. Typical values of these parameters in our runs are $\delta_1 = 0.2$ and $\delta_2 = 0.075$. We can freely adjust the coefficient c_β in (8); $c_\beta = 0.6$ works well for us (note that the typical value in $4D$ simulations is $c_\beta = 0.75$). Following [9], we introduce diffusion terms (well inside the apparent horizon) on the right hand side of the equations of motion for those variables that appear with second spatial derivatives. This improves the stability of our code, especially

in the rapidly spinning regime. See [9] for more details. We use Kreiss-Oliger dissipation [24] to damp unphysical high-frequency modes that can arise at grid boundaries or during regridding, with typical dissipation values of $\sigma = 0.4$. We numerically solve the CCZ4 equations using the GRChombo libraries [25, 26], using up to 9 levels of refinement, with a 2:1 refinement ratio, and typically 140^3 points on the coarsest grid. We consider a cubic computational domain, with side length $L = 200$. The x and y are standard Cartesian coordinates, with infinite range, which we cut off at some finite values; we typically impose periodic boundary conditions (BCs) for simplicity, but we have also experimented with Sommerfeld BCs and the results are essentially the same. Needless to say, our choice of BCs limits the duration of our simulations. The z coordinate has range $0 \leq z \leq L$; at $z = 0$ we impose regularity as derived from the cartoon method, and at $z = L$ we impose either periodic or Sommerfeld BCs. We discretize the equations using fourth order finite differences, and integrate in time using RK4. We obtain approximately 3^{rd} order convergence, see Appendix §G for convergence tests.

We also track the apparent horizon (AH) during several stages of the evolution, see [9]; our apparent horizon finder assumes that the AH is a star-shaped surface. Whilst this is sufficient to describe the AH for the low spin runs, this assumption breaks down when the deformations are too large. In this case, one would need to use a more general parametrization of the AH along the lines of [14] or more recently [27]. We leave this for future work. However, as in [9], we verify that in our working gauge, certain contours of χ track the AH to within a few percent. Thus we can use χ to get a good approximation of the location and shape of the AH. In Appendix §F we verify this claim with cases where the AH satisfies our star-shaped assumption, and can thus be calculated and compared to contours of χ .

B. Gravitational wave extraction

One of the aims of this article is to provide a general picture of higher dimensional black hole instabilities and their endpoints. To this end, the gravitational waves that are emitted during the evolution of these instabilities are a valuable source of insight. We are able to do this in two ways: the first is to extract the h_+ and h_\times components of the metric perturbations at a certain radius along the z -axis [15, 16]:

$$h_+ = \frac{\tilde{\gamma}_{xx} - \tilde{\gamma}_{yy}}{2} \left(\frac{z}{\mu^{1/(D-3)}} \right)^{\frac{D-2}{2}}, \quad (9)$$

$$h_\times = \tilde{\gamma}_{xy} \left(\frac{z}{\mu^{1/(D-3)}} \right)^{\frac{D-2}{2}}. \quad (10)$$

As noted in these references, h_+ and h_\times basically contain the same information. This method has the advantage that it is very easy to implement and it accurately captures the $m = 2$ modes, allowing us to compare our results with the existing results in the literature [16, 17]. However, this approach misses the higher m modes and in particular the $m = 4$

³ In practice this time scale is exponential, and much faster than the physical timescale of the instabilities.

⁴ The preferred choice in the typical $4D$ astrophysical setting is $c_\alpha = 2$.

mode that becomes the dominant one at larger spins. Note that the perturbative calculations of [17] only consider modes with $m = 2$. Therefore, for this work, we have implemented a completely general approach to gravitational wave extraction in higher dimensions based on the higher dimensional analogues of the Newman-Penrose scalars introduced in [20]. We follow the implementation of [28] to calculate the non-vanishing components of the Weyl tensor along the outgoing null rays, $\Omega'_{(A)(B)}$. For the class of spacetimes that we consider, the non-vanishing components of $\Omega'_{(A)(B)}$ are [28]:

$$\Omega'_{(\hat{i})(\hat{j})} = \frac{1}{2} \left[R_{0k0l} m_{(\hat{i})}^k m_{(\hat{j})}^l - R_{mk0l} m_{(\hat{i})}^m m_{(\hat{i})}^k m_{(\hat{j})}^l - R_{0kml} m_{(\hat{i})}^k m_{(\hat{i})}^m m_{(\hat{j})}^l + R_{mknl} m_{(\hat{i})}^m m_{(\hat{i})}^k m_{(\hat{i})}^n m_{(\hat{j})}^l \right], \quad (11)$$

$$\Omega'_{(\hat{a})(\hat{b})} = \delta_{(\hat{a})(\hat{b})} \frac{1}{2\gamma_{ww}} \left[R_{w0w0} - 2R_{w0wk} m_{(\hat{1})}^k - R_{wkwl} m_{(\hat{1})}^k m_{(\hat{1})}^l \right], \quad (12)$$

where the indices $i, j = 2, 3$ run along the spatial angular dimensions of the computational domain and the indices \hat{a}, \hat{b}, \dots run along the transverse sphere. Here R_{0klm} etc. denote the components of the spacetime Riemann tensor, $m_{(\hat{i})}^i$ is the unit radial vector and $m_{(\hat{i})}^k$ are the angular unit vectors. To construct an orthonormal basis of vectors, we start from

$$\begin{aligned} m_{(1)} &= x \partial_x + y \partial_y + z \partial_z, \\ m_{(2)} &= -(y^2 - z^2) \partial_x + x y \partial_y + x z \partial_z, \\ m_{(3)} &= -z \partial_y + y \partial_z, \end{aligned} \quad (13)$$

and use the standard Gram-Schmidt orthonormalization procedure. Changing to spherical coordinates as in (B2), one can show that as $r \rightarrow \infty$, the basis orthonormalized vectors approaches,

$$\begin{aligned} m_{(\hat{1})} &= \frac{1}{r} \partial_r, \\ m_{(\hat{2})} &= \frac{1}{r} \partial_{\theta_n}, \\ m_{(\hat{3})} &= \frac{1}{r \sin \theta_n} \partial_{\theta_{n-1}}. \end{aligned} \quad (14)$$

The unit vectors along the transverse sphere directions are simply given by,

$$m_{(\hat{a})} = \frac{1}{\sqrt{\gamma_{ww}}} \partial_{w_a}. \quad (15)$$

We extract the individual modes in the gravitational wave signal by projecting $\Omega'_{(A)(B)}$ onto a basis of tensor harmonics on the sphere at infinity:

$$\Omega'_{\ell\dots} = \lim_{r \rightarrow \infty} r^{\frac{D-2}{2}} \int d\Omega_{(n)} Y_{\ell\dots}^{(A)(B)*} \Omega'_{(A)(B)} \quad (16)$$

where $\ell\dots$ denotes the set of quantum numbers that identify each of the harmonics, and $d\Omega_{(n)}$ is the volume element on the

round unit sphere S^n . In this article we focus on the $n = 3, 4$ cases but the procedure is completely general. In practice we carry out the extraction at several radii to verify that we are in the wave zone. Whilst a basis for tensor harmonics on S^3 is known, see e.g., [29], to the best of our knowledge, our results for tensor harmonics on S^4 are new. See Appendix §D. Needless to say, for the $m = 2$ modes, both methods give the same frequencies and growth/decay rates within our numerical errors⁵.

III. RESULTS

We now present results for the non-linear evolution of non-axisymmetric perturbations of singly spinning black holes in $5D$ and $6D$. The dynamics of MP black holes in $7D$ is qualitatively similar to the $6D$ case, and some of the most relevant results are deferred to the appendices. We start by discussing the $5D$ case in §III A, where we resolve the existing tension in the literature regarding the stability/instability of MP BHs with a sufficiently large spin. We move on in §III B to study the non-linear stability properties of $6D$ MP BHs of various spins: in §III B 1 we study the gravitational waveforms and extract the quasinormal modes (QNMs), in §III B 2 we study the physics of the apparent horizon (AH), and in §III B 3 we discuss the endpoint of the instabilities for large angular momentum.

In the following, we will use several geometric measures of the AH to estimate the mass and spin of the black hole throughout the evolution, even though the relations between the geometry of the horizon and the physical quantities of the black hole are only valid for equilibrium configurations. The following relations between the MP parameters and the horizon are valid in the stationary configuration

$$r_h = \left(\frac{A}{C} \frac{2\pi}{\Omega_{D-2}} \right)^{\frac{1}{D-3}}, \quad \mu_h = \frac{C}{2\pi} r_h^{D-4}, \quad a_h = r_h \sqrt{\frac{\mu_h}{r_h^{D-3}} - 1} \quad (17)$$

with A the horizon's area and C its equatorial circumference. In the dynamical regime, eq. (17) defines r_h , μ_h and a_h . Note that our results scale with the chosen length scale μ , related to the black-hole mass of the initial configuration. As the evolution proceeds, we dynamically re-scale the physical quantities according to the lengths μ_h and r_h . For instance, non-linear dynamics that settles to a final MP BH in $6D$ results in a final, dimensionless spin of $(a/\mu^{1/3})_{\text{final}} = a_h/\mu_h^{1/3}$.

⁵ To calculate the QNMs, we first extract the exponential growth/decay rates by fitting a straight line over the envelope of local extrema in the log-linear plot of the given data. The errors associated with this step are mainly due to the particular time interval chosen. The early and late data are contaminated by junk radiation and accumulated numerical error, respectively, whereas the signal shows a transition from growing to decaying regimes for intermediary times. Next, we use the information of the growth/decay rates to obtain a purely sinusoidal signal, from which we read the oscillatory frequency via a Fourier transformation. Here, the accuracy is restricted to the wavelengths available in the signal.

Before we proceed, we remind the reader of some well-known properties of singly spinning MP BHs in $D \geq 5$ spacetime dimensions. See [30] and references therein for more details. For fixed total mass, in $5D$ the angular momentum of an MP BH is bounded from above by an extremal bound; configurations saturating this bound have a naked ring singularity. This situation should be contrasted with the Kerr family of solutions, for which the solution saturating the Kerr bound correspond to an extremal black hole with a degenerate horizon. On the other hand, for $D \geq 6$, the angular momentum is unbounded from above and for any finite angular momentum, the black hole horizon is non-degenerate and has finite area.

A. Case $D = 5$

In Ref. [15], the non-linear dynamics of rapidly spinning MP BHs in 5 spacetime dimensions were studied for the first time, under perturbations that break the axial symmetry along the rotation plane whilst preserving the transverse $U(1)$. They found that for values of $a/\mu^{1/2} \sim 0.87$, there exists an exponentially growing mode that induces a bar-shaped deformation on the AH i.e. an unstable $m = 2$ mode. The authors found that the growth of the instability appeared to be stronger for larger values of $a/\mu^{1/2}$. However, the non-linear evolution of the instability was not followed, so determining the endpoint of the instability remained an open problem. On the other hand, Ref. [17] studied perturbations of singly spinning MP BHs in $D \geq 5$ with $m \geq 2$. In the $D = 5$ case, the results of [17] indicate that all linear modes decay exponentially, which would lead one to conclude that MP BHs are linearly stable in $5D$, at least for the values of the spin parameters that were studied numerically. The results of [15] and [17] would be compatible if the instability is non-linear.

Here we revisit the results from [15] by carrying out analogous fully non-linear simulations of perturbed MP BHs with various values of the spin parameter, and in particular for values of $a/\mu^{1/2}$ for which [15] observed an instability. When comparing our results to those in [15], one should note that although our gauge choice is different, our method of perturbing the black hole is essentially the same as the one used in this reference.

Contrary to the results in [15], we find that all rapidly spinning black holes in $5D$ that we are able to simulate are non-linearly stable. For a perturbed black hole with $a/\mu^{1/2} = 0.89$ for instance, Fig. 1 shows the gravitational waveform extracted on the z axis [15] at $z_0/\mu^{1/2} = 21.5$. The plot below shows the $(\ell_3, m) = (2, 2)$ scalar multipole of the gravitational waveform extracted from $\Omega'_{(A)(B)}$. From the damped oscillatory decay, we obtain a dominant QNM with frequency $\omega\mu^{1/2} = 1.283 - 0.032i$, which agrees with the results from perturbation theory of [17], i.e. $\omega r_+ = 0.585 - 0.015i$. As a further check, we computed the the frequency and decay rate of the leading QNM from both h_+ and $\Omega'_{(A)(B)}$, and they agree within truncation error.

In $5D$ we find that gravitational waveform is essentially in the $(\ell_3, m) = (2, 2)$ scalar derived sector, see Fig. 1. The projection onto the other tensor harmonics, i.e., vector derived

and transverse traceless tensors, gives waveforms with amplitudes that are smaller than those in the $\ell_4 = 2$ scalar sector by one order of magnitude or more. Higher multipoles again give much smaller waveforms.

Our results together with the results of [17] suggest that $5D$ MP BHs are both perturbatively and non-perturbatively stable under perturbations that break the axial symmetry on the rotation plane. In this article, we do not study the stability properties of MP BHs with values of $a/\mu^{1/2}$ that are arbitrarily close to extremality. As pointed out in [31], the dynamics of the Kerr black holes near extremality can exhibit turbulence, so it is conceivable that similar dynamics will arise for MP BHs in the limit $a/\mu^{1/2} \rightarrow 1$.

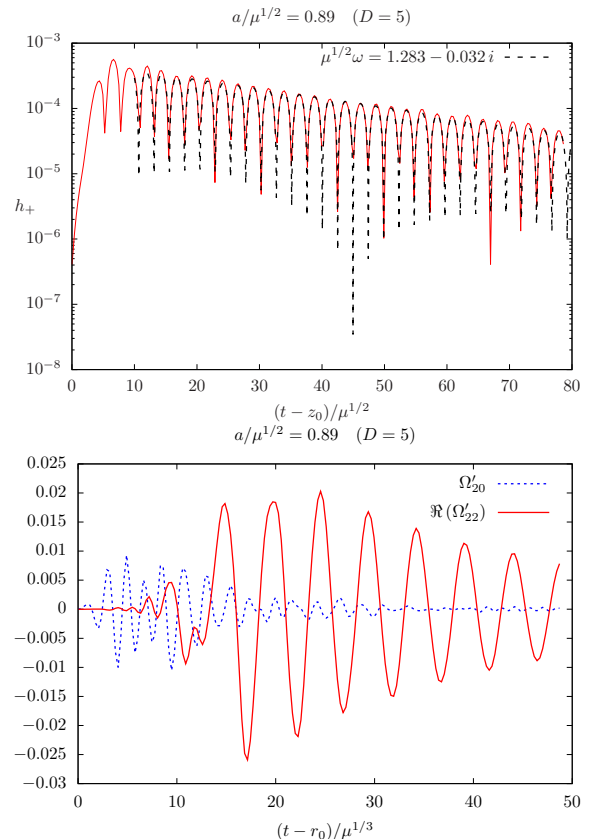


FIG. 1. *Top*: gravitational waveform extracted from h_+ measured at a finite radius along the z -axis. The red line is the actual data whilst the dashed line is our best fit, corresponding to the values of the frequency and decay rate shown in the inset. *Bottom*: $(\ell_3, m) = (2, 0)$ and the real part of the $(\ell_3, m) = (2, 2)$ scalar derived multipoles of $\Omega'_{(A)(B)}$ extracted at a finite radius. Clearly, most of the signal is in the $m = 2$ mode.

B. Case $D = 6$

In this subsection we consider the non-linear evolution of perturbed $6D$ MP BHs of different values of the spin parameter $a/\mu^{1/3}$. The results in $7D$ are qualitatively similar and we

will not show them here.

Recall that in $D \geq 6$, the dimensionless spin parameter $a/\mu^{1/3}$ of singly spinning MP BHs can be arbitrarily large. Ref. [10] noted that the thermodynamics of spinning black holes exhibits a qualitative change in behaviour as the angular momentum increases beyond a certain (dimension dependent) critical value of $a_{\text{crit}}/\mu^{1/(D-3)}$; for values of $a/\mu^{1/(D-3)}$ smaller than this critical value, MP BHs behave similarly to the Kerr black hole, and for values of $a/\mu^{1/(D-3)}$ greater than this critical value they behave like black membranes. In $6D$, one finds $a_{\text{crit}}/\mu^{1/3} \simeq 1.29$ and the ultraspinning instability kicks in at $a/\mu^{1/3} \simeq 1.57$ [32]. The endpoints of certain ultraspinning instability were worked out in [14]. On the other hand, the non-axisymmetric instabilities of $6D$ MP BHs kick in at $a/\mu^{1/3} \simeq 0.74$ [16, 17]. In this article we study the endpoint of non-axisymmetric instabilities for MP BHs with $0.7 \leq a/\mu^{1/3} \leq 1.5$. The results presented here, taken in conjunction with those in [14], constitute a complete picture of the dynamics of singly spinning MP BHs.

1. Gravitational Waves

In Table I we summarize the QNM frequencies in the $m = 2$ sector that we have extracted from our fully non-linear simulations. To obtain the results displayed on this table, we considered sufficiently small perturbations, with amplitudes $A = 0.02$. Although our simulations are fully non-linear, thus making it difficult to obtain accurate results for linear waves, our results agree within truncation error with the perturbative calculations of [17]. On the left column of Table I we display the normalized frequencies of the leading mode obtained from perturbing the initial black hole with an $m = 2$ mode. This shows that black holes with $a/\mu^{1/3} = 0.7$ are stable, while for $a/\mu^{1/3} \geq 0.8$ the sign of the imaginary part of the frequency indicates a linear instability. In the right column we display the normalized frequencies of the leading QNM in the ring down phase for those runs that settle back onto another MP BH. We measured the AH area and the length of the circumference of the AH on the equatorial plane of the final state to estimate the mass and angular momentum parameter of the final MP black hole using (17). These results indicate that all runs settle down to the *same* black hole, independent of the initial value of $a/\mu^{1/3}$ that we have considered.

In Fig. 2 (top) we display the gravitational waveforms corresponding to black holes with initial spin $a/\mu^{1/3} = 1.3$, extracted using the metric perturbations. Together with the waveforms, we also display snapshots of the AH at different stages of the evolution as an inset above the figure. From these AH snapshots, it is clear that the dynamics is governed by an $m = 2$ mode which deforms the AH into a bar shape. The black hole radiates mass and angular momentum until it spins down and settles down to an equilibrium MP BH, with lower mass and angular momentum. In Fig. 2 (middle) and (bottom) we show the gravitational waveforms extracted from the Weyl scalars for both $\ell_4 = 2$ and $\ell_4 = 4$ modes in the scalar derived sector of tensor harmonics. Most of the signal is in the $(\ell_4, m) = (2, 2)$ mode, but the $\ell_4 = 4$ also displays a

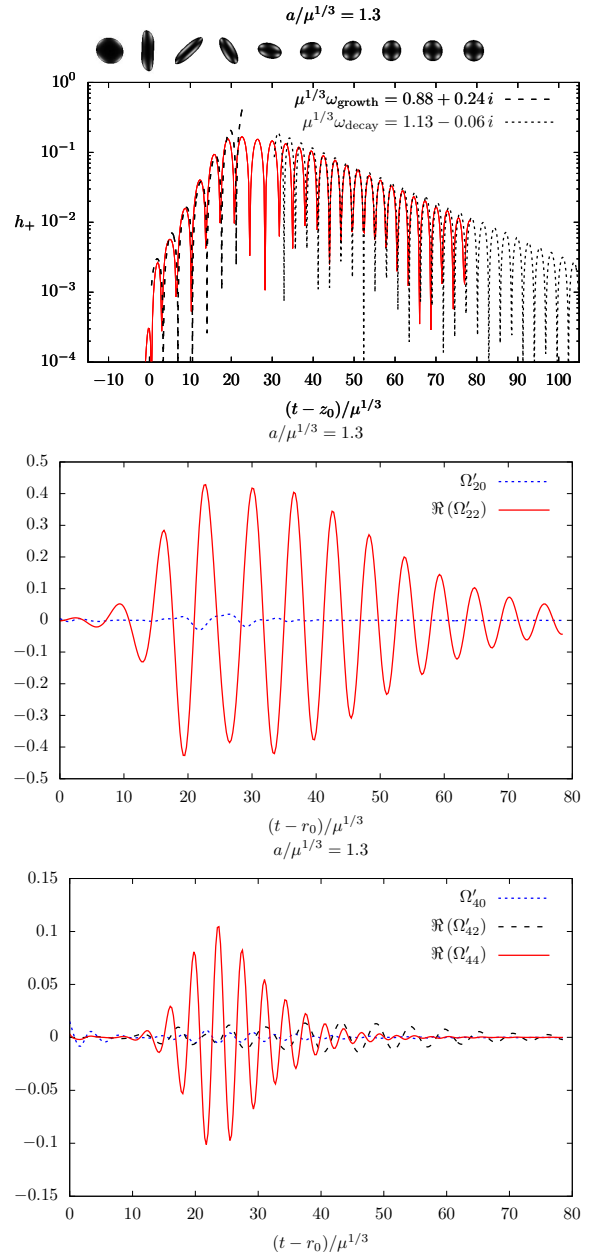


FIG. 2. *Top*: Gravitational wave ($m = 2$ mode) at $z_0/\mu^{1/3} = 21.5$, together with snapshots of the apparent horizon for initial spin parameter $a/\mu^{1/3} = 1.3$. The dashed and dotted lines provide the fit for the QNMs in the growing and decaying phases. Table I displays the frequencies normalized w.r.t the initial/final horizon scales. *Middle and Bottom*: Gravitational waveforms obtained from the higher dimensional Weyl scalars projected on a sphere at finite radius: $(\ell_4, m) = (2, 0)$ and the real part of the $(\ell_4, m) = (2, 2)$ modes (*middle*) and $(\ell_4, m) = (4, 0)$ and real parts of the $(\ell_4, m) = (4, 2), (4, 4)$ modes (*bottom*). Most of the signal lies on the $(\ell_4, m) = (2, 2)$ mode, but higher harmonics are also excited due to the non-linearities.

Initial state		Final state		Mass/spin loss	
$a_h/\mu_h^{1/3}$	$\omega_{22}\mu_h^{1/3}$	$a_h/\mu_h^{1/3}$	$\omega_{22}\mu_h^{1/3}$	$\Delta(\mu_h/r_h^3)$	$\Delta(a_h/\mu_h^{1/3})$
0.7	$1.07 - 0.03i$	0.7	$1.07 - 0.03i$	—	—
0.8	$1.03 + 0.03i$	xxx	xxx	xxx	xxx
0.9	$1.03 + 0.07i$	0.66	$1.04 - 0.03i$	34.0%	25.5%
1.0	$1.00 + 0.12i$	0.64	$1.08 - 0.05i$	48.0%	34.3%
1.1	$0.95 + 0.17i$	0.64	$1.06 - 0.05i$	60.0%	41.2%
1.2	$0.91 + 0.21i$	0.63	$1.05 - 0.05i$	69.6%	46.0%
1.3	$0.88 + 0.24i$	0.63	$1.05 - 0.05i$	77.3%	50.2%
1.4	$0.82 + 0.26i$	0.63	$1.05 - 0.05i$	83.5%	54.0%

TABLE I. Real and Imaginary parts of the leading quasinormal modes in the $(\ell_4, m) = (2, 2)$ sector of gravitational perturbations. *Left*: from perturbing the initial black hole. For $a/\mu^{1/3} = 0.7$ black holes are stable, while for $a/\mu^{1/3} \geq 0.8$ black holes are unstable. *Right*: leading QNM in the ring down phase. For all initial values of $a/\mu^{1/3}$ that end up settling back to an MP BH, we find that the end state is the same black hole. For $a/\mu^{1/3} = 1.5$, the endpoint of the instability is a naked singularity. We estimate an error of ± 0.02 in the real and imaginary part of the frequencies (see footnote 5)

sizeable signal. However, for MP BHs with $a/\mu^{1/3} = 1.3$ the $(\ell_4, m) = (2, 2)$ mode governs the non-linear evolution.

The endpoint of the evolution of these instabilities depends, in a non-trivial way, on the amplitude of the initial perturbation and the value of $a/\mu^{1/3}$ for the initial black hole. For small enough perturbations and small enough initial value of $a/\mu^{1/3}$, the end state of the non-axisymmetric instabilities is another MP BH. Surprisingly, the perturbed black holes of this type that we have been able to simulate all settle down to the *same* MP BH, the one with $(a/\mu^{1/3})_{\text{final}} = 0.63$. We are not aware of the physical reason that singles out this particular member of the MP family, but our simulations suggest that it behaves as an attractor. It would be worth investigating this point further.

2. Apparent Horizon

In Fig. 3 we display the evolution of the estimated black hole mass and spin parameter from the geometry of the AH, (17). These estimates only correspond to the mass and spin parameter of a black hole in equilibrium, and therefore they are exact only at the initial and final stages of the evolution. However, they indicate that highly spinning unstable black holes can radiate an enormous amount of mass and angular momentum due to the large deformation of the horizon during the highly non-linear stages of the evolution. For instance, black holes with an initial $a/\mu^{1/3} = 1.3$ can radiate up to 77% of the initial mass and 50% of the initial spin. This should be contrasted with the head on collisions of black holes in higher dimensions, for which less than 1% of the total mass is radiated [33, 34] (in $D = 6$, the fraction of mass radiated is $(8.19 \pm 0.05) \times 10^{-4}$), or in the first black hole binary merger recorded by LIGO [1], which radiated roughly 4.6% of the initial mass into gravitational waves. In Fig. 4 we display three snapshots of the AH during the evolution of a perturbed MP with initial $a/\mu^{1/3} = 1.3$. As can be seen

from these snapshots, the AH develops a strong bar-shaped type of deformation, which leads to a very strong emission of gravitational radiation. As the plots in Fig. 3 show, the amount of mass and angular momentum radiated increases with the initial value of $a/\mu^{1/3}$, so it is conceivable that one can achieve even higher emission percentages for larger initial values $a/\mu^{1/3}$. However, as we will discuss next, there may be a (dimension dependent) dynamical upper bound due to the fact that the generic endpoint of the evolution of the instability of MP BH with a sufficiently large initial value of $a/\mu^{1/3}$ or a sufficiently large initial deformation is no longer another MP BH, but is a naked singularity.

3. Large initial spin

Given the large deformations observed at moderate spins and small perturbations, e.g., see Fig. 4, one may wonder what happens when the spin of the unperturbed black hole or the size of the deformation is increased. In this article, we are interested in the end points of perturbative instabilities of black holes, so we will always keep the initial deformation small enough to remain in the perturbative regime initially and vary the spin of the MP BH. As we now show, the inevitable endpoint of the instabilities for sufficiently rapidly spinning black holes is a naked singularity. Before we proceed, note that as the deformations of the AH beyond spherical symmetry become increasing large during the highly non-linear stages of the evolution, the AH ceases to be a star-shaped surface which is an assumed property underlying the AH finder we use. The same situation was shown to occur in unstable black rings [9] or in the ultraspinning instability of MP black holes [14]. The latter reference managed to find non-star-shaped AH using an intrinsic parametrization of the surface, whilst [27] proposed the use of a reference surface. We will leave the interesting problem of implementing one of these methods to the present situation for future work. However, as in [9, 14], we have

Initial state $a_h/\mu_h^{1/3} = 1.3$		Final state $a_h/\mu_h^{1/3} = 0.63$	
$\omega_{42}\mu_h^{1/3}$	$\omega_{44}\mu_h^{1/3}$	$\omega_{42}\mu_h^{1/3}$	$\omega_{44}\mu_h^{1/3}$
$1.70 + 0.36i$	$1.61 + 0.40i$	$1.68 - 0.12i$	$1.83 - 0.13i$

TABLE II. Real and imaginary parts of the sub-leading $(\ell_4, m) = (4, 2)$ and $(\ell_4, m) = (4, 4)$ quasinormal mode for $m = 2$ perturbation of an MP BH with the initial configuration $a/\mu^{1/3} = 1.3$. We estimate an error of ± 0.04 in the real and imaginary part of the frequencies (see footnote5).

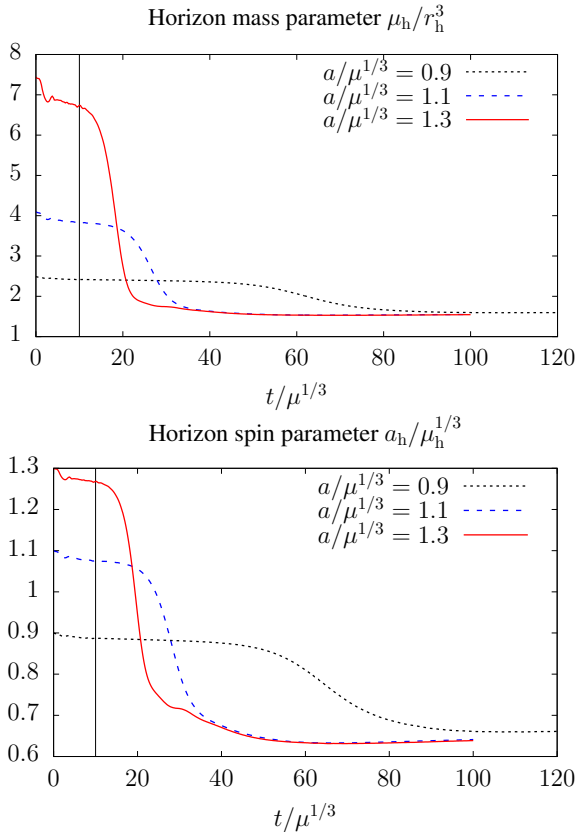


FIG. 3. Dynamical evolution of horizon measures for initial MP BHs with $a/\mu^{1/3} = 0.9$ (dotted black), μ_h for $a/\mu^{1/3} = 1.1$ (dashed blue) and $a/\mu^{1/3} = 1.3$ (continuous red). *Top*: Normalized horizon mass parameter μ_h/r_h^3 . *Bottom*: Normalized spin parameter $a_h/\mu_h^{1/3}$. MP BHs radiate enormous amount of mass and angular momentum. The vertical line indicates the time around which the initial gauge dynamics settles down.

verified that certain contours of the conformal factor χ provide a very accurate description of the AH, within less than a few percent. See Appendix §F for quantitative comparison between the contours of χ and the actual AH for various runs where the latter can be found. Therefore, we will use contours of χ as approximations of AH for situations where the latter is not a star-shaped surface, and hence get intuition of

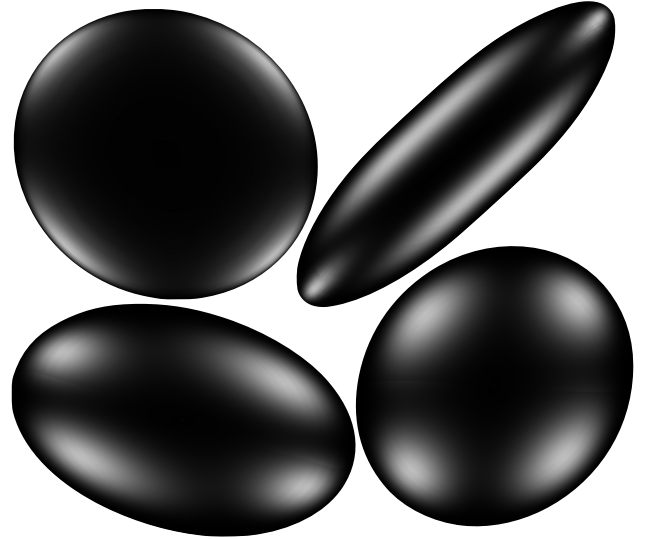


FIG. 4. Snapshots of AH during the evolution of an unstable MP BH with initial $a/\mu^{1/3} = 1.3$ and perturbation amplitude $A = 0.02$. There is a strong bar-shaped deformation during the highly non-linear stages of the evolution. Gravitational waves eventually radiate away the non-axisymmetric deformations and the black hole settles to another member of the MP family, with lower angular momentum.

the physics of the instabilities and their endpoints.⁶

For MP BH's with an initial $a/\mu^{1/3} = 1.5$, we find that numerical noise is enough to excite the $m = 4$ mode, which is the one that dominates the subsequent non-linear evolution.⁷ Table III displays the quasinormal frequencies in the $(\ell_4, m) = (4, 4)$ sector for $a/\mu^{1/3} = 1.5$. Modes with $m = 2$ which are present in the noise also get excited but have much smaller amplitude. See Fig. 5. Comparing the waveforms of the $m = 4$ instability for $a/\mu^{1/3} = 1.5$ in Fig. 5 with their counterpart waveforms for the $m = 2$ instability for $a/\mu^{1/3} = 1.3$ in Fig. 2, notice that the amplitude for the

⁶ Note that since contours of χ provide accurate approximations of the AH, in principle one could use them as suitable reference surfaces to find the AH using the method of [27].

⁷ The same happens for black rings: moderately thin rings are unstable under a GL mode with $m = 2$, while for sufficiently thin rings the fastest growing instability is in $m = 4$ sector. Presumably, for even thinner rings, higher m modes are more unstable, just as in the GL instability of black strings.

Initial state $a_h/\mu_h^{1/3} = 1.5$	
$\omega_{42}\mu_h^{1/3}$	$\omega_{44}\mu_h^{1/3}$
$1.71 + 0.34i$	$1.68 + 0.34i$

TABLE III. Real and imaginary parts of the leading $(\ell_4, m) = (4, 2)$ and $(\ell_4, m) = (4, 4)$ quasinormal mode for $m = 4$ perturbation of a MP BH with the initial configuration $a/\mu^{1/3} = 1.5$. We estimate an error of ± 0.04 in the real and imaginary part of the frequencies (see footnote5). No information of the final stage is available as the evolution leads to the formation of naked singularities.

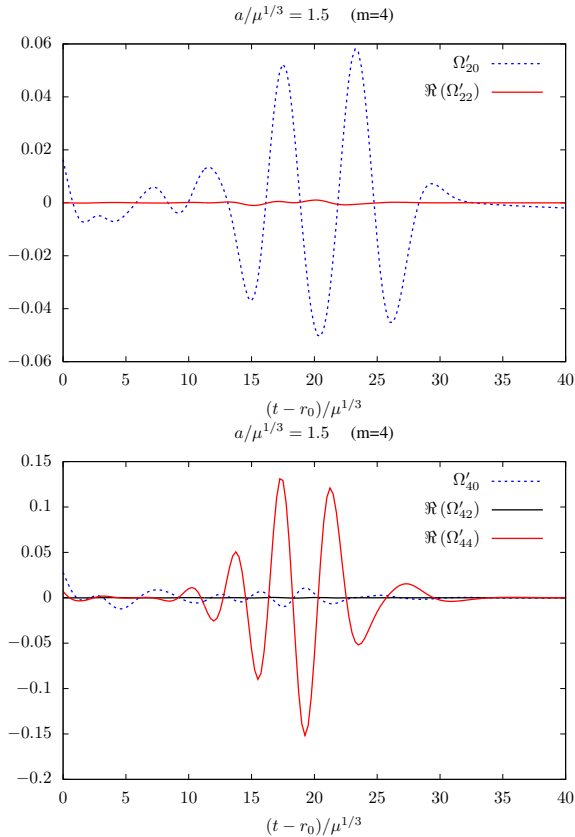


FIG. 5. Gravitational waveforms obtained during the evolution of an unstable MP BH with initial $a/\mu^{1/3} = 1.5$, with the instability triggered by numerical noise. *Top:* $(\ell_4, m) = (2, 0)$ and the real part of the $(\ell_4, m) = (2, 2)$ modes. *Bottom:* $(\ell_4, m) = (4, 0)$ and the real part of the $(\ell_4, m) = (4, 2), (4, 4)$ modes. Most of the signal is in the $m = 4$ mode, but the $m = 2$ modes are also present. Note the difference in amplitude between this run and the $a/\mu^{1/3} = 1.3$ one, Fig. 2. This suggests that at higher spins, gravitational wave emission becomes less efficient and instabilities have time to develop and eventually form a naked singularity. This run crashes close to the singularity but we artificially froze the evolution around the black hole to extract the gravitational waves. Therefore, the part of the waveform after $(t - r_0)/\mu^{1/2} \sim 23$ is unphysical.

$m = 2$ case is much larger, even though the AH deformation is quite extreme in both cases. This suggests that efficiency of the gravitational wave emission during the evolution of the instabilities decreases as $a/\mu^{1/3}$ increases, hence giving

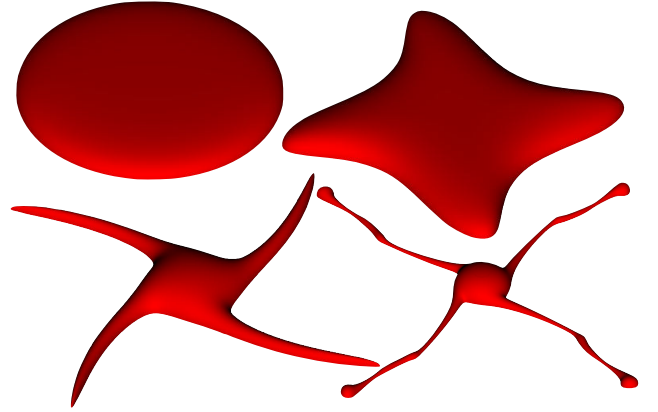


FIG. 6. Snapshots of the $\chi = 0.5$ contour during the evolution of an unstable MP BH with initial $a/\mu^{1/3} = 1.5$ and no initial perturbation. This contour tracks the AH very closely, see Appendix §F. The evolution is dominated by an $m = 4$ present in the numerical noise. During the evolution, the black hole develops a square shape and the tips of the square eventually grow into long arms. The latter eventually become GL unstable. The last snapshot shows the second generation bulge propagating along the arm, a characteristic feature of GL dynamics.

more time for these instabilities to grow and eventually form a naked singularity. The simple physical reason for this is that the structures that form at large values of $a/\mu^{1/3}$, as deformed as they may be, contain only a small amount of the total mass.

In Fig. 6 we show representative snapshots of $\chi = 0.5$ contours from the evolution of the MP BH with $a/\mu^{1/3} = 1.5$. The initial deformation of the black hole horizon into a square shape is characteristic of the $m = 4$ mode. Subsequently, as the instability develops, the corners of the square grow into four arms. These arms become longer and thinner as time goes by, until at some point a local GL instability kicks in along the arms, signalled by the appearance of a bulge in the central part of each of the arms. These bulges travel outwards towards the tip of the arms due to centrifugal force, which leads to a further thinning of arms, and mass accumulates at the tips, forming nearly spherical bulges. It becomes very difficult to continue the simulation beyond this point since resolving the new generations of bulges that form due to the lo-



FIG. 7. Snapshots of the $\chi = 0.5$ contour during the evolution of an unstable MP BH with initial $a/\mu^{1/3} = 1.5$ and an initial $m = 2$ perturbation with amplitude $A = 0.1$. The evolution is dominated by the $m = 2$ mode, but $m = 4$ modes excited by the numerical noise are also present. In the non-linear regime, the black hole develops a bar shape, which gets longer over time and pointy at the tip. In analogy with the $m = 4$ case, the appearance of pointy tips precedes the formation of long and thin arms, which eventually become GL unstable. We suspect that this is the most likely fate of this evolution.

cal GL instability becomes computationally very expensive.⁸ However, the local evolution of the instability along each of the arms appears to be analogous to the ultraspinning case of [14]. In this case, it was observed that the interaction between the centrifugal force and mass accretion by the big bulges accelerates the formation of a naked singularity compared to the GL instability of black strings [5], and the process is no longer self-similar. Note that the central bulge becomes more spherical as the evolution proceeds and in fact contains most of the mass of the system. This explains why the gravitational wave emission is less efficient at this stage of the evolution, at sufficiently large values of $a/\mu^{1/3}$. We believe that this is a generic aspect of the dynamics of unstable black holes at large angular momentum. The most likely end point of this instability is that quantum gravity effects will govern the break-up of the arms, and the resulting four black holes will either fly off to infinity or be recaptured by the central black hole.

If we start with a black hole with initial $a/\mu^{1/3} = 1.5$ and perturb it with an $m = 2$ mode, we can in principle explore the non-linear evolution of this sector of perturbations at large angular momentum. It turns out that choosing an initial $m = 2$ perturbation with amplitude of $A = 0.02$ is sufficient to ensure that these modes dominate the non-linear regime. In this case, we find that during the highly non-linear regime of the subsequent evolution, the AH becomes more elongated and develops very sharp features at the edges, see Fig. 7. The appearance of these sharp features is not a numerical artefact and

it makes the numerical simulation of the system very difficult. Whilst we were unable to continue this particular simulation beyond this point due to the cost of the computation, one is tempted to conjecture that the endpoint of the evolution may well be a naked singularity. Indeed, the spacetime curvature at these sharp tips grows large, as spatial gradients diverge and the time scales become very fast. In fact, in the $m = 4$ case, the appearance of the sharp tips precedes the formation of long and thin arms, which eventually become GL unstable. We suspect that the same will happen in the present $m = 2$ case: it is quite possible that the evolution will continue by forming two long arms, joined at a central region that is nearly spherical and contains most of the mass. These long arms will become thinner over time due to the centrifugal force and eventually will develop local GL instabilities. Therefore, the endpoint of the evolution is likely the formation of a naked singularity in finite asymptotic time.

IV. DISCUSSION

In this article we describe the evolution and endpoints of non-axisymmetric perturbations of singly spinning MP BHs in $5D$ and $6D$. In the $5D$ case, we find that all black holes that we have considered are non-linearly stable, thus resolving the tension between the numerical simulations of [15] and the perturbation theory results of [17]. In the $6D$ case we found that slowly spinning black holes are stable. As the initial spin increases, at around $a/\mu^{1/3} \approx 0.8$ MP BHs become unstable under perturbations with an $m = 2$ azimuthal mode number (i.e., bar-mode), as [16] had previously observed and [17] confirmed. We have been able to evolve MP BHs with significantly larger initial spins than previous works, and the picture that has emerged is the following: in the non-linear regime, unstable black holes develop a bar-shape which leads to a strong emission of gravitational waves, through which the black hole eventually settles back down to another member of the MP family with a lower angular momentum. See Fig. 4. As the initial spin of the black hole grows, the amount of mass and angular momentum emitted by the gravitational waves during the evolution also grows, reaching a staggering 83% of radiated mass for a black hole with initial spin $a/\mu^{1/3} = 1.4$. This is much larger than previously observed in head on collisions of black holes in higher dimensions. It would be interesting to explore whether these high emission rates have implications for scenarios with large extra dimensions. Another surprising fact uncovered in this work is that *all* unstable MP BHs that settle back down to another member of the MP family in fact seem to settle onto the *same* black hole, the MP BH with $a/\mu^{1/3} = 0.63$. Therefore, this particular member of the MP family seems to be an attractor, at least for the evolution of unstable BHs under a bar mode type of deformation. We do not have a physical explanation for this behavior since the $a/\mu^{1/3} = 0.63$ black hole does not have any particular physical properties that single it out among nearby solutions. It would be very interesting to understand why this particular solution seems to be special.

For initial spins of $a/\mu^{1/3} \approx 1.5$, it is the $m = 4$ mode that

⁸ Recall that the PDEs that we are solving are effectively $(3 + 1)$ -dimensional, while in [5] or [14] the system is $(2 + 1)$ -dimensional, thus allowing one to get much closer to the singularity.

has the fastest growth rate and will generically dominate the subsequent evolution, even though lower m modes are still present. The same situation was observed in the case of the black ring in $5D$ [9]. The evolution of these instabilities is different than those at lower spins; the $m = 4$ mode results in a square type deformation, which then evolves into four arms, see Fig. 6. These arms grow longer and thinner over time, until they eventually develop a local GL instability. In this article we have been able to follow the evolution of this local instability beyond the formation of the first generation of bulges. After this point the simulation becomes too computationally expensive. However, at this point the fate of these black holes is sealed: the development of the GL instability is at least exponential in time, whilst the emission of gravitational waves only follows a power law. Therefore, once the local GL instability kicks in, a naked singularity will inevitably form in finite asymptotic time before the unlucky black hole has had time to radiate away enough mass and angular momentum. Since this mechanism is generic, one may interpret this as further evidence that the weak cosmic censorship conjecture is false in higher dimensional asymptotically flat spacetimes. Note that it is not clear whether the type of singularity that forms is visible to external far away observers and hence whether it constitutes an honest violation of the conjecture. To settle this issue, one would need to analyse the (in)completeness of null infinity, which remains an open question for this class of spacetimes. However, arbitrarily large curvatures near the horizon do become visible. Since the mass contained in these regions of increasingly large curvature becomes negligible over time, the potential violation of the weak cosmic censorship conjecture would be of the mildest possible type in the language of [35]. For these rapidly spinning black holes, one can also trigger an instability in the $m = 2$ sector of perturbations. Even though we were not able to follow the evolution to the point of seeing the appearance of local GL instabilities and hence naked singularities, it seems that this is the most likely endpoint.

The instabilities discussed in this article are of the “elastic” type [9], as opposed to GL type of instabilities. Intuitively, elastic instabilities deform the black hole horizon without introducing substantial thicknesses variations. GL instabilities in singly spinning MP BHs kick in at slightly larger spins, $a/\mu^{1/3} = 1.572$ in $D = 6$ [32]; the evolution and endpoints of the latter were studied in [14]. Whether the elastic type of instabilities or the GL ones dominate the evolution of a given black hole is a question of suitably preparing the initial conditions. We do not see any obstruction in being able to construct open sets of initial conditions for which either the elastic or GL instability dominates the subsequent evolution by exciting the desired mode with a sufficiently large initial amplitude. Therefore, this article together with [14] provide a complete picture of the dynamics of some of the most notable instabilities that afflict MP black holes and their respective endpoints.⁹

One important result in higher dimensional black hole physics that emerges from our work is that sufficiently rapidly rotating black holes in higher dimensions are unstable and evolve into a naked singularity in finite time as a result of local GL dynamics, regardless of the nature of the original instability. Both the elastic and GL instabilities are quite generic in the sense that they should afflict other types of higher dimensional black holes apart from MP BHs and black rings. This leads us to the following statement. **Conjecture:** *the GL instability is the only mechanism that higher dimensional vacuum GR has to change the topology of a black hole horizon in dynamical spacetimes.* If true, this conjecture would make the detailed understanding of the GL instability an even more pressing issue. The fact that the GL instability in black strings appears to be self-similar and perhaps controlled by an attractor offers hope that some analytic progress is possible in this case.

The dynamics of singly spinning MP BHs in $7D$ is qualitatively and quantitatively very similar to the $6D$ ones. Namely, BHs are non-linear stable for sufficiently small angular momentum. At larger spins, they first become unstable under a bar mode type of deformation. The evolution of this instability again ends on another member of the MP family, with lower mass and spin. For larger angular momentum, the $m = 4$ mode becomes the fastest growing unstable mode and the endpoint is a naked singularity, which forms in finite asymptotic time. The only difference between $6D$ and $7D$ is that naked singularities appear to form at lower values of the angular momentum. For instance, in $7D$, the $a/\mu^{1/4} = 1.3$ MP BH is unstable under an $m = 4$ mode and the endpoint of the instability is a naked singularity. As a rule of thumb, it seems that forming naked singularities is “easier” as D increases.

One may object that unstable BHs should not be regarded as “generic” and consequently the potential violations of the weak cosmic censorship conjecture in this and previous works should not be considered generic. First, the question of whether it is possible or not to construct open sets of initial conditions sufficiently close to the unstable black holes considered in these works remains open. Second, in this article we have shown that black holes with sufficiently large angular momentum develop local GL instabilities which inevitably end up forming naked singularities. Last but not least, using the large D limit of GR, Ref. [35] provided compelling evidence that it should be possible to generically form single black holes with large angular momentum by colliding black holes with a non-zero impact parameter. Moreover, this reference also suggested that these black holes should evolve into naked singularities via local GL instabilities. In this article we have shown that these local GL instabilities do indeed kick in when one expects them to do so. It now remains to show that indeed the scenario put forward in [35] is realized in finite D . $D = 6$ should suffice.

ACKNOWLEDGMENTS

We would like to thank Tomas Andrade, Jay Armas, Roberto Emparan, Mahdi Godazgar, Harvey Reall and Ulrich

⁹ The superradiant instability is another important instability that affects these black holes, but we have not considered it here.

Sperhake for discussions. We have benefited from being part of the GRChombo collaboration (www.grchombo.org), our special thanks go to the whole collaboration. HB, PF, MK and RPM were supported by the European Research Council Grant No. ERC-2014- StG 639022-NewNGR “New frontiers in numerical general relativity”. PF is also supported by a Royal Society University Research Fellowship (Grant No. UF140319). We acknowledge that the results of this research have been achieved using the DECI resource Cartesius based in the Netherlands with support from the PRACE DECI-14-Tier-1 call. Some of the computations reported in this article were also performed at the MareNostrum4 super-computer at the Barcelona Supercomputing Centre, grants no.

FI-2019-1-0010, FI-2018-3-0004, FI-2017-3-0012, FI-2017-2-0018, FI-2017-1-0042. We also acknowledge the use of Athena at HPC Midlands+, which was funded by the EPSRC on grant EP/P020232/1, in this research, as part of the HPC Midlands+ consortium. Part of this work was performed using the Cambridge Service for Data Driven Discovery (CSD3), part of which is operated by the University of Cambridge Research Computing on behalf of the STFC DiRAC HPC Facility (www.dirac.ac.uk). The DiRAC component of CSD3 was funded by BEIS capital funding via STFC capital grants ST/P002307/1 and ST/R002452/1 and STFC operations grant ST/R00689X/1. DiRAC is part of the National e-Infrastructure

-
- [1] B. P. Abbott *et al.* (LIGO Scientific, Virgo), *Phys. Rev. Lett.* **116**, 061102 (2016).
- [2] K. Akiyama *et al.* (Event Horizon Telescope), *Astrophys. J.* **875**, L1 (2019).
- [3] R. P. Kerr, *Phys. Rev. Lett.* **11**, 237 (1963).
- [4] R. Gregory and R. Laflamme, *Phys. Rev. Lett.* **70**, 2837 (1993).
- [5] L. Lehner and F. Pretorius, *Phys. Rev. Lett.* **105**, 101102 (2010).
- [6] R. Emparan and H. S. Reall, *Phys. Rev. Lett.* **88**, 101101 (2002).
- [7] A. A. Pomeransky and R. A. Sen’kov, (2006).
- [8] J. E. Santos and B. Way, *Phys. Rev. Lett.* **114**, 221101 (2015).
- [9] P. Figueras, M. Kunesch, and S. Tunyasuvunakool, *Phys. Rev. Lett.* **116**, 071102 (2016).
- [10] R. Emparan and R. C. Myers, *JHEP* **09**, 025 (2003).
- [11] R. Emparan, T. Harmark, V. Niarchos, and N. A. Obers, *Phys. Rev. Lett.* **102**, 191301 (2009).
- [12] O. J. C. Dias, P. Figueras, R. Monteiro, J. E. Santos, and R. Emparan, *Phys. Rev. D* **80**, 111701 (2009).
- [13] O. J. C. Dias, P. Figueras, R. Monteiro, H. S. Reall, and J. E. Santos, *JHEP* **05**, 076 (2010).
- [14] P. Figueras, M. Kunesch, L. Lehner, and S. Tunyasuvunakool, *Phys. Rev. Lett.* **118**, 151103 (2017).
- [15] M. Shibata and H. Yoshino, *Phys. Rev. D* **81**, 021501 (2010).
- [16] M. Shibata and H. Yoshino, *Phys. Rev. D* **81**, 104035 (2010).
- [17] O. J. C. Dias, G. S. Hartnett, and J. E. Santos, *Class. Quant. Grav.* **31**, 245011 (2014).
- [18] F. Pretorius, *Class. Quant. Grav.* **22**, 425 (2005).
- [19] W. G. Cook, P. Figueras, M. Kunesch, U. Sperhake, and S. Tunyasuvunakool, *Proceedings, 3rd Amazonian Symposium on Physics: Belem, Brazil, September 28-October 2, 2015*, *Int. J. Mod. Phys. D* **25**, 1641013 (2016).
- [20] M. Godazgar and H. S. Reall, *Phys. Rev. D* **85**, 084021 (2012).
- [21] D. Alic, C. Bona-Casas, C. Bona, L. Rezzolla, and C. Palenzuela, *Phys. Rev. D* **85**, 064040 (2012).
- [22] A. Weyhausen, S. Bernuzzi, and D. Hilditch, *Phys. Rev. D* **85**, 024038 (2012).
- [23] D. Alic, W. Kastaun, and L. Rezzolla, *Phys. Rev. D* **88**, 064049 (2013).
- [24] H. Kreiss, H. Kreiss, J. Olinger, and G. A. R. P. J. O. Committee, *Methods for the approximate solution of time dependent problems*, GARP publications series (International Council of Scientific Unions, World Meteorological Organization, 1973).
- [25] K. Clough, P. Figueras, H. Finkel, M. Kunesch, E. A. Lim, and S. Tunyasuvunakool, *Class. Quant. Grav.* **32**, 245011 (2015), [*Class. Quant. Grav.* **32**, 24(2015)].
- [26] M. Adams *et al.*, (2015).
- [27] D. Pook-Kolb, O. Birnholtz, B. Krishnan, and E. Schnetter, *Phys. Rev. D* **99**, 064005 (2019).
- [28] W. G. Cook and U. Sperhake, *Class. Quant. Grav.* **34**, 035010 (2017).
- [29] L. Lindblom, N. W. Taylor, and F. Zhang, *Gen. Rel. Grav.* **49**, 139 (2017).
- [30] R. Emparan and H. S. Reall, *Living Rev. Rel.* **11**, 6 (2008).
- [31] H. Yang, A. Zimmerman, and L. Lehner, *Phys. Rev. Lett.* **114**, 081101 (2015).
- [32] O. J. C. Dias, P. Figueras, R. Monteiro, and J. E. Santos, *Phys. Rev. D* **82**, 104025 (2010).
- [33] H. Witek, M. Zilhao, L. Gualtieri, V. Cardoso, C. Herdeiro, A. Nerozzi, and U. Sperhake, *Phys. Rev. D* **82**, 104014 (2010).
- [34] W. G. Cook, U. Sperhake, E. Berti, and V. Cardoso, *Phys. Rev. D* **96**, 124006 (2017).
- [35] T. Andrade, R. Emparan, D. Licht, and R. Luna, *JHEP* **04**, 121 (2019).
- [36] H. Bondi, M. G. J. van der Burg, and A. W. K. Metzner, *Proc. Roy. Soc. Lond.* **A269**, 21 (1962).
- [37] R. K. Sachs, *Proc. Roy. Soc. Lond.* **A270**, 103 (1962).
- [38] K. Tanabe, S. Kinoshita, and T. Shiromizu, *Phys. Rev. D* **84**, 044055 (2011).
- [39] M. Durkee, V. Pravda, A. Pravdova, and H. S. Reall, *Class. Quant. Grav.* **27**, 215010 (2010).
- [40] A. Chodos and E. Myers, *Annals Phys.* **156**, 412 (1984).
- [41] M. A. Rubin and C. R. Ordonez, *J. Math. Phys.* **26**, 65 (1985).
- [42] A. Higuchi, *J. Math. Phys.* **28**, 1553 (1987), [Erratum: *J. Math. Phys.* **43**, 6385(2002)].
- [43] L. Gualtieri, E. Berti, V. Cardoso, and U. Sperhake, *Phys. Rev. D* **78**, 044024 (2008).
- [44] E. Berti, V. Cardoso, and M. Casals, *Phys. Rev. D* **73**, 024013 (2006), [Erratum: *Phys. Rev. D* **73**, 109902(2006)].

Appendix A: Asymptotic flatness and gravitational waves

We assume the spacetime to be asymptotically flat in the sense of [20]. Thus, in the wave zone, the line element is expressed in the Bondi-Sachs form [36, 37]

$$ds^2 = -\mathcal{A}e^{\mathcal{B}} du^2 - 2e^{\mathcal{B}} du dr + r^2 h_{\alpha\beta} (d\phi^\alpha + \mathcal{C}^\alpha) (d\phi^\beta + \mathcal{C}^\beta), \quad (\text{A1})$$

with u a retarded time and, \mathcal{A} , \mathcal{B} , \mathcal{C}^α and $h_{\alpha\beta}$ functions on the Bondi-coordinate (u, r, ϕ^α) . Moreover, $\det h_{\alpha\beta} = \det \omega_{\alpha\beta}$,

where $\omega_{\alpha\beta}$ is the unit metric on the unit n -sphere S^n . Here, we are interested in the asymptotic expansion [38]

$$h_{\alpha\beta}(u, r, \phi^\gamma) = \omega_{\alpha\beta}(\phi^\gamma) + \sum_{s \geq 1} \frac{h_{\alpha\beta}^{(s)}(u, \phi^\gamma)}{r^{D/2+s-2}}. \quad (\text{A2})$$

with $h_{\alpha\beta}^{(1)}$ the Bondi news function.

We consider the higher-dimensional generalisation of the Geroch-Held-Penrose (GHP) formalism [39] and introduce a tetrad basis (ℓ, k, m_A) satisfying $\ell^\mu k_\mu = 1$, $m_{(A)}^\mu m_{(B)\mu} = \delta_{(A)(B)}$, and with vanishing further contractions. Asymptotically, one particular choice for the tetrad is

$$\begin{aligned} \ell &= -\partial_r, & k &= \partial_u - \frac{1}{2}\partial_r \\ m_{(1)} &= r^{-1}\partial_\theta & m_{(2)} &= (r \sin \theta)^{-1}\partial_\varphi \\ m_{(a)} &= \left(r \cos \theta \prod_{b=4}^{a-1} \sin(\phi^b) \right)^{-1} \partial_{\phi^a} & a &= 4 \cdots D-1 \end{aligned} \quad (\text{A3})$$

Gravitational waves are extracted from the projection of the Weyl tensor $C_{\mu\nu\rho\sigma}$ onto the tetrad basis (A3). Specifically, the news function $h_{\alpha\beta}^{(1)}$ is given by the leading contribution of [20],

$$\Omega'_{AB} = C_{\mu\nu\rho\sigma} k^\mu m_{(A)}^\nu k^\rho m_{(B)}^\sigma \quad (\text{A4})$$

$$= -\frac{m_{(A)}^\mu m_{(B)}^\nu \ddot{h}_{\mu\nu}^{(1)}}{2r^{D/2-1}} + \mathcal{O}(r^{-D/2}). \quad (\text{A5})$$

From the symmetries of $C_{\mu\nu\rho\sigma}$, one verifies that Ω'_{AB} is symmetric and traceless.

Appendix B: Spherical harmonics on a n -sphere

In this appendix we collect some well-known properties of spherical harmonics on an S^n . In Appendices §C and §D we specialize to the cases of interest for us, namely S^3 and S^4 .

We start by setting up our notation and conventions.¹⁰ Following [28], we consider spherical coordinates $Y^A = (t, r, \theta_a)$ which relate to a Cartesian coordinate system $X^a = (t, w_i)$ via

$$\begin{aligned} w_1 &= r \cos(\theta_n), \\ w_2 &= r \sin(\theta_n) \cos(\theta_{n-1}), \\ w_3 &= r \sin(\theta_n) \sin(\theta_{n-1}) \cos(\theta_{n-2}), \\ &\vdots \\ w_{D-2} &= r \sin(\theta_n) \cdots \sin(\theta_2) \cos(\theta_1), \\ w_{D-1} &= r \sin(\theta_n) \cdots \sin(\theta_2) \sin(\theta_1). \end{aligned} \quad (\text{B1})$$

Here, $\theta_1 \in [0, 2\pi]$ and $\theta_a \in [0, \pi] \forall a = 2 \dots, n$. In the 3-dimensional computational domain, we parametrize the numerical Cartesian coordinates (x, y, z) by new spherical coordinates (r, θ, φ) via

$$\begin{aligned} x &= r \cos(\theta_n), \\ y &= r \sin(\theta_n) \cos(\theta_{n-1}), \\ z &= r \sin(\theta_n) \sin(\theta_{n-1}), \end{aligned} \quad (\text{B2})$$

with $\theta_n, \theta_{n-1} \in [0, \pi]$.

Now we are in position to collect some properties of scalar harmonics and higher rank tensor harmonics on an arbitrary n -sphere S^n , with $n > 2$. Ultimately we are interested in tensor harmonics on the S^3 and the S^4 . Whilst the former are well-known, see e.g., [29] and references therein, our results for the tensor harmonics on the S^4 are, to the best of our knowledge, new.

We write down the metric ds_n^2 on the unit round S^n as

$$\begin{aligned} ds_1^2 &= d\theta_1^2, \\ ds_i^2 &= d\theta_i^2 + \sin^2 \theta_i ds_{i-1}^2, \quad i = 2, \dots, n, \end{aligned} \quad (\text{B3})$$

with $0 \leq \theta_1 \leq 2\pi$ and $0 \leq \theta_i \leq \pi, \forall i = 2, \dots, n$. We refer to this particular form of the metric on the S^n as the ‘‘standard’’ form and the corresponding basis of unit vectors as the ‘‘standard’’ basis.

Recall that spherical harmonics on the unit S^n are defined as eigenfunctions of the Laplace operator on the S^n :¹¹

$$\nabla^a \nabla_a \mathbb{S}^{\ell_n, \dots, \ell_1} = -\ell_n(\ell_n + n - 1) \mathbb{S}^{\ell_n, \dots, \ell_1}, \quad (\text{B4})$$

where the integers ℓ_i satisfy $\ell_n \geq \ell_{n-1} \geq \dots \geq \ell_2 \geq |\ell_1|$. The scalar harmonics are normalized so that

$$\delta_{\ell_n \ell'_n \dots \ell_1 \ell'_1} = \int_{S^n} \mathbb{S}^{\ell_n, \dots, \ell_1} \mathbb{S}'^{\ell'_n, \dots, \ell'_1}, \quad (\text{B5})$$

where the volume element of S^n is omitted to avoid clutter. From the scalar harmonics, one can construct scalar derived vector harmonics on the S^n . These are given by

$$\mathbb{S}_a^{\ell_n, \dots, \ell_1} = \frac{1}{\sqrt{\ell_n(\ell_n + n - 1)}} \nabla_a \mathbb{S}^{\ell_n, \dots, \ell_1}, \quad (\text{B6})$$

and they satisfy:

$$\nabla^b \nabla_b \mathbb{S}_a^{\ell_n, \dots, \ell_1} = [-\ell_n(\ell_n + n - 1) + n - 1] \mathbb{S}_a^{\ell_n, \dots, \ell_1}, \quad (\text{B7})$$

$$\nabla^a \mathbb{S}_a^{\ell_n, \dots, \ell_1} = -\sqrt{\ell_n(\ell_n + n - 1)} \mathbb{S}^{\ell_n, \dots, \ell_1}, \quad (\text{B8})$$

$$\delta_{\ell_n \ell'_n \dots \ell_1 \ell'_1} = \int_{S^n} g^{ab} \mathbb{S}_a^{\ell_n, \dots, \ell_1} \mathbb{S}_b'^{\ell'_n, \dots, \ell'_1}, \quad (\text{B9})$$

¹⁰ Upper case latin indices A, B, \dots run from 0 to $D - 1$. Lower case latin letters i, j, \dots are spatial indices running from 1 to $D - 1$ and greek letters denote angular indices from 2 to $D - 1$. The sphere has dimension $K = D - 2$ and the computation domain has $d = 3$ spatial dimensions.

¹¹ Here we work on the unit S^n . One can easily reinstate the radius in our formulas.

where g is the metric on the round unit S^n . On the other hand, divergence free vector harmonics $\mathbb{V}_a^{\ell_n, \dots, \ell_1}$ on the S^n satisfy

$$\nabla^b \nabla_b \mathbb{V}_a^{\ell_n, \dots, \ell_1} = [-\ell_n(\ell_n + n - 1) + 1] \mathbb{V}_a^{\ell_n, \dots, \ell_1}, \quad (\text{B10})$$

$$\nabla^a \mathbb{V}_a^{\ell_n, \dots, \ell_1} = 0, \quad (\text{B11})$$

$$\delta_{\ell_n \ell'_n \dots \ell_1 \ell'_1} = \int_{S^n} g^{ab} \mathbb{V}_a^{\ell_n, \dots, \ell_1} \mathbb{V}_b^{\ell'_n, \dots, \ell'_1}. \quad (\text{B12})$$

One can show that there are $n-1$ linearly independent, orthogonal and divergence free vector harmonics on the S^n which, together with the scalar derived vector harmonics (B6), form a complete basis of vectors on the S^n , see [40–42].

From the scalar harmonics (B4), one can obtain two types of symmetric tensor harmonics:

$$\mathbb{S}_{(1)ab}^{\ell_n, \dots, \ell_1} = \frac{1}{\sqrt{n}} g_{ab} \mathbb{S}^{\ell_n, \dots, \ell_1}, \quad (\text{B13})$$

$$\mathbb{S}_{(2)ab}^{\ell_n, \dots, \ell_1} = \frac{\sqrt{n}}{\sqrt{(n-1)(\ell_n-1)(\ell_n+n-1)}} \left(\nabla_a \mathbb{S}_b^{\ell_n, \dots, \ell_1} + \frac{\sqrt{\ell_n(\ell_n+n-1)}}{n} g_{ab} \mathbb{S}^{\ell_n, \dots, \ell_1} \right) \quad (\text{B14})$$

These satisfy:

$$\nabla^c \nabla_c \mathbb{S}_{(1)ab}^{\ell_n, \dots, \ell_1} = -\ell_n(\ell_n + n - 1) \mathbb{S}_{(1)ab}^{\ell_n, \dots, \ell_1} \quad (\text{B15})$$

$$\nabla^a \mathbb{S}_{(1)ab}^{\ell_n, \dots, \ell_1} = -\frac{\sqrt{\ell_n(\ell_n+n-1)}}{\sqrt{n}} \mathbb{S}_b^{\ell_n, \dots, \ell_1}, \quad (\text{B16})$$

$$g^{ab} \mathbb{S}_{(1)ab}^{\ell_n, \dots, \ell_1} = \sqrt{n} \mathbb{S}_{(1)ab}^{\ell_n, \dots, \ell_1}, \quad (\text{B17})$$

$$\delta_{\ell_n \ell'_n \dots \ell_1 \ell'_1} = \int_{S^n} g^{ac} g^{bd} \mathbb{S}_{(1)ab}^{\ell_n, \dots, \ell_1} \mathbb{S}_{(1)cd}^{\ell'_n, \dots, \ell'_1}. \quad (\text{B18})$$

On the other hand, we have

$$\nabla^c \nabla_c \mathbb{S}_{(2)ab}^{\ell_n, \dots, \ell_1} = [-\ell_n(\ell_n + n - 1) + 2n] \mathbb{S}_{(2)ab}^{\ell_n, \dots, \ell_1} \quad (\text{B19})$$

$$\nabla^a \mathbb{S}_{(2)ab}^{\ell_n, \dots, \ell_1} = -\frac{\sqrt{(n-1)(\ell_n-1)(\ell_n+n)}}{\sqrt{n}} \mathbb{S}_b^{\ell_n, \dots, \ell_1}, \quad (\text{B20})$$

$$g^{ab} \mathbb{S}_{(2)ab}^{\ell_n, \dots, \ell_1} = 0, \quad (\text{B21})$$

$$\delta_{\ell_n \ell'_n \dots \ell_1 \ell'_1} = \int_{S^n} g^{ac} g^{bd} \mathbb{S}_{(2)ab}^{\ell_n, \dots, \ell_1} \mathbb{S}_{(2)cd}^{\ell'_n, \dots, \ell'_1}. \quad (\text{B22})$$

Recall that the matrix of Weyl scalars, Ω'_{AB} , encoding the gravitational radiation is symmetric and traceless. Therefore, the family $\mathbb{S}_{(1)ab}$ of scalar derived tensor harmonics cannot contribute to the multipolar expansion of the Weyl scalars. Hence, from now on we will only consider the second family, $\mathbb{S}_{(2)ab}$, of scalar derived tensor harmonics and we shall drop the subscript (2) .

From each family of vector harmonics, one can similarly construct the corresponding family of vector derived tensor harmonics:

$$\mathbb{V}_{ab}^{\ell_n, \dots, \ell_1} = \frac{1}{\sqrt{2(\ell_n-1)(\ell_n+n)}} \left(\nabla_a \mathbb{V}_b^{\ell_n, \dots, \ell_1} + \nabla_b \mathbb{V}_a^{\ell_n, \dots, \ell_1} \right) \quad (\text{B23})$$

These satisfy,

$$\nabla^c \nabla_c \mathbb{V}_{ab}^{\ell_n, \dots, \ell_1} = [-\ell_n(\ell_n + n - 1) + n + 2] \mathbb{V}_{ab}^{\ell_n, \dots, \ell_1}, \quad (\text{B24})$$

$$\nabla^a \mathbb{V}_{ab}^{\ell_n, \dots, \ell_1} = -\frac{\sqrt{(\ell_n-1)(\ell_n+n)}}{\sqrt{2}} \mathbb{V}_b^{\ell_n, \dots, \ell_1}, \quad (\text{B25})$$

$$g^{ab} \mathbb{V}_{ab}^{\ell_n, \dots, \ell_1} = 0, \quad (\text{B26})$$

$$\delta_{\ell_n \ell'_n \dots \ell_1 \ell'_1} = \int_{S^n} g^{ac} g^{bd} \mathbb{V}_{ab}^{\ell_n, \dots, \ell_1} \mathbb{V}_{cd}^{\ell'_n, \dots, \ell'_1}. \quad (\text{B27})$$

Finally, transverse traceless symmetric tensor harmonics are defined by,

$$\nabla^c \nabla_c \mathbb{T}_{ab}^{\ell_n, \dots, \ell_1} = [-\ell_n(\ell_n + n - 1) + 2] \mathbb{T}_{ab}^{\ell_n, \dots, \ell_1}, \quad (\text{B28})$$

$$\nabla^a \mathbb{T}_{ab}^{\ell_n, \dots, \ell_1} = 0, \quad (\text{B29})$$

$$g^{ab} \mathbb{T}_{ab}^{\ell_n, \dots, \ell_1} = 0, \quad (\text{B30})$$

$$\delta_{\ell_n \ell'_n \dots \ell_1 \ell'_1} = \int_{S^n} g^{ac} g^{bd} \mathbb{T}_{ab}^{\ell_n, \dots, \ell_1} \mathbb{T}_{cd}^{\ell'_n, \dots, \ell'_1}. \quad (\text{B31})$$

Needless to say, the different families of tensor harmonics are orthogonal to each other and together form a complete basis of tensor harmonics on the S^n .

The class of dynamical spacetimes that we consider possess a transverse round S^{n-2} . Therefore, to extract the gravitational waveforms form the components of the Weyl scalars we can restrict ourselves to tensor harmonics on the S^n that preserve an internal $\text{SO}(n-1)$ symmetry. This amounts to assuming that $\ell_{n-2} = \dots = \ell_1 = 0$ for the quantum numbers labelling the harmonics. We shall restrict to this class of harmonics from now on.

Appendix C: Tensor harmonics on the S^3

In this Appendix we collect some results on tensor harmonics on the S^3 .

1. Standard basis

We write the round metric on the unit S^3 as:

$$ds^2 = d\theta_3^2 + \sin^2 \theta_3 (d\theta_2^2 + \sin^2 \theta_2 d\theta_1^2), \quad (\text{C1})$$

with $\theta_3, \theta_2 \in [0, \pi]$ and $\theta_1 \in [0, 2\pi]$. We choose the following basis of unit vectors on the S^3 :

$$m_{(1)} = \frac{\partial}{\partial \theta_3}, \quad m_{(2)} = \frac{1}{\sin \theta_3} \frac{\partial}{\partial \theta_2}, \quad m_{(3)} = \frac{1}{\sin \theta_3 \sin \theta_2} \frac{\partial}{\partial \theta_1} \quad (\text{C2})$$

In this basis, the projected components of the harmonics with $\ell_1 = 0$ are:¹²

¹² Since tensor harmonics are symmetric $\mathbb{Y}_{21}^{\ell_1 \dots} = \mathbb{Y}_{12}^{\ell_1 \dots}$ so we do not need to list all components.

a. *Scalar derived tensor harmonics*

- $(\ell_3, \ell_2) = (2, 0)$:

$$\begin{aligned}\mathbb{S}_{11}^{(2,0)} &= -\frac{2}{\pi} \sqrt{\frac{2}{15}} \sin^2(\theta_3), \\ \mathbb{S}_{22}^{(2,0)} &= \frac{1}{\pi} \sqrt{\frac{2}{15}} \sin^2(\theta_3), \\ \mathbb{S}_{33}^{(2,0)} &= \frac{1}{\pi} \sqrt{\frac{2}{15}} \sin^2(\theta_3).\end{aligned}\quad (\text{C3})$$

- $(\ell_3, \ell_2) = (2, 1)$:

$$\begin{aligned}\mathbb{S}_{11}^{(2,1)} &= -\frac{1}{\sqrt{5}\pi} \sin(2\theta_3) \cos(\theta_2), \\ \mathbb{S}_{12}^{(2,1)} &= \frac{3}{2\sqrt{5}\pi} \sin(\theta_3) \sin(\theta_2), \\ \mathbb{S}_{22}^{(2,1)} &= \frac{1}{2\sqrt{5}\pi} \sin(2\theta_3) \cos(\theta_2), \\ \mathbb{S}_{33}^{(2,1)} &= \frac{1}{2\sqrt{5}\pi} \sin(2\theta_3) \cos(\theta_2).\end{aligned}\quad (\text{C4})$$

- $(\ell_3, \ell_2) = (2, 2)$:

$$\begin{aligned}\mathbb{S}_{11}^{(2,2)} &= -\frac{1}{4\sqrt{15}\pi} (\cos(2\theta_3) + 2)(3 \cos(2\theta_2) + 1), \\ \mathbb{S}_{12}^{(2,2)} &= \frac{3}{4\pi} \sqrt{\frac{3}{5}} \cos(\theta_3) \sin(2\theta_2), \\ \mathbb{S}_{22}^{(2,2)} &= \frac{1}{8\sqrt{15}\pi} [3 \cos(2\theta_2)(\cos(2\theta_3) + 5) + \cos(2\theta_3) - 7], \\ \mathbb{S}_{33}^{(2,2)} &= \frac{1}{2\sqrt{15}\pi} [(4 - 3 \cos^2(\theta_2)) \sin^2(\theta_3) + 3 \cos^2(\theta_3)].\end{aligned}\quad (\text{C5})$$

b. *Vector derived tensor harmonics* There are two families of vector derived tensor harmonics on the S^3 , but given the class of spacetimes that we consider in this article, only one of them has a non-zero overlap with the Weyl scalars. The relevant vector harmonics for us are given by:

- $(\ell_3, \ell_2) = (2, 1)$

$$\begin{aligned}\mathbb{V}_{11}^{(2,1)} &= \frac{4}{\sqrt{15}\pi} \sin(\theta_3) \cos(\theta_2), \\ \mathbb{V}_{12}^{(2,1)} &= -\frac{1}{2\pi} \sqrt{\frac{3}{5}} \sin(2\theta_3) \sin(\theta_2), \\ \mathbb{V}_{22}^{(2,1)} &= -\frac{2}{\sqrt{15}\pi} \sin(\theta_3) \cos(\theta_2), \\ \mathbb{V}_{33}^{(2,1)} &= -\frac{2}{\sqrt{15}\pi} \sin(\theta_3) \cos(\theta_2).\end{aligned}\quad (\text{C6})$$

- $(\ell_3, \ell_2) = (2, 2)$

$$\begin{aligned}\mathbb{V}_{11}^{(2,2)} &= \frac{1}{\sqrt{15}\pi} [3 \cos(2\theta_2) + 1] \cos(\theta_3), \\ \mathbb{V}_{12}^{(2,2)} &= -\frac{1}{4\pi} \sqrt{\frac{3}{5}} \sin(2\theta_2) [3 + \cos(2\theta_3)], \\ \mathbb{V}_{22}^{(2,2)} &= -\frac{1}{\sqrt{15}\pi} [3 \cos(2\theta_2) - 1] \cos(\theta_3), \\ \mathbb{V}_{33}^{(2,2)} &= -\frac{2}{\sqrt{15}\pi} \cos(\theta_3).\end{aligned}\quad (\text{C7})$$

c. *Transverse traceless tensor harmonics* There are two families of transverse traceless tensor harmonics on the S^3 but, as with the vectors, only one of them has a non-zero overlap with the Weyl tensor. This is given by:

- $(\ell_3, \ell_2) = (2, 2)$

$$\begin{aligned}\mathbb{T}_{11}^{(2,2)} &= -\frac{1}{2\sqrt{6}\pi} [3 \cos(2\theta_2) + 1], \\ \mathbb{T}_{12}^{(2,2)} &= \frac{1}{2\pi} \sqrt{\frac{3}{2}} \sin(2\theta_2) \cos(\theta_3), \\ \mathbb{T}_{22}^{(2,2)} &= \frac{1}{\sqrt{6}\pi} \left[\cos^2(\theta_2) - \frac{1}{2} \sin^2(\theta_2) (3 \cos(2\theta_3) + 1) \right], \\ \mathbb{T}_{33}^{(2,2)} &= \frac{1}{4\sqrt{6}\pi} [6 \sin^2(\theta_2) \cos(2\theta_3) + 3 \cos(2\theta_2) + 1].\end{aligned}\quad (\text{C8})$$

2. Adapted basis

Given the symmetries of the spacetimes that we consider, it seems more natural to write the metric on the S^3 as follows:

$$ds^2 = d\chi^2 + \sin^2 \chi d\phi^2 + \cos^2 \chi d\psi^2, \quad (\text{C9})$$

with $\chi \in [0, \pi/2]$ and $\phi, \psi \in [0, 2\pi]$. Indeed, in this form, the rotation axis in the spacetime coincides with the ϕ direction in (C9). Written in these coordinates, scalar harmonics on the S^3 are given by

$$\begin{aligned}Y^{\ell_3, m, \bar{m}} &= C_{\ell_3}^{m+, m-} e^{i(m\phi + \bar{m}\psi)} \\ &\times (1 - \cos 2\chi)^{\frac{|m|}{2}} (1 + \cos 2\chi)^{\frac{|\bar{m}|}{2}} \\ &\times P_{\frac{\ell_3}{2} - m_+}^{(m, \bar{m})}(\cos 2\chi),\end{aligned}\quad (\text{C10})$$

where $m = m_+ + m_-$, $\bar{m} = m_+ - m_-$, $P_n^{(a,b)}(x)$ is the Jacobi polynomial and

$$C_{\ell_3}^{m_+, m_-} = \frac{1}{2^{m_+} \pi} \sqrt{\frac{\ell_3 + 1}{2}} \sqrt{\frac{(\ell_3/2 + m_+)! (\ell_3 - m_+)!}{(\ell_3/2 + m_-)! (\ell_3 - m_-)!}} \quad (\text{C11})$$

with $|m_{\pm}| \leq \frac{\ell_3}{2}$ and $\frac{\ell_3}{2} - m_{\pm} \in \mathbb{N}$.

Given the symmetries of spacetimes that we are considering, we are interested in harmonics with $\bar{m} = 0$. We consider

the obvious basis of vectors on the S^3 given the form of the metric in (C9),

$$m_{(1)} = \frac{\partial}{\partial \chi}, \quad m_{(2)} = \frac{1}{\sin \chi} \frac{\partial}{\partial \phi}, \quad m_{(3)} = \frac{1}{\cos \chi} \frac{\partial}{\partial \psi}, \quad (\text{C12})$$

In this basis, the scalar derived tensor harmonics on the S^3 with $\ell_3 = 2$ are given by:

- $(\ell_3, m) = (2, 0)$

$$\begin{aligned} \mathbb{S}_{11}^{(2,0)} &= -\frac{1}{\sqrt{10}\pi} \cos(2\chi), \\ \mathbb{S}_{22}^{(2,0)} &= \frac{1}{2\sqrt{10}\pi} [\cos(2\chi) - 3], \\ \mathbb{S}_{33}^{(2,0)} &= \frac{1}{2\sqrt{10}\pi} [\cos(2\chi) + 3]. \end{aligned} \quad (\text{C13})$$

- $(\ell_3, m) = (2, 2)$

$$\begin{aligned} \mathbb{S}_{11}^{(2,2)} &= \frac{1}{2\sqrt{10}\pi} e^{2i\phi} [\cos(2\chi) + 2], \\ \mathbb{S}_{12}^{(2,2)} &= \frac{3i}{2\sqrt{10}\pi} e^{2i\phi} \cos(\chi), \\ \mathbb{S}_{22}^{(2,2)} &= -\frac{1}{4\sqrt{10}\pi} e^{2i\phi} [\cos(2\chi) + 5], \\ \mathbb{S}_{33}^{(2,2)} &= \frac{1}{2\sqrt{10}\pi} e^{2i\phi} \sin^2(\chi). \end{aligned} \quad (\text{C14})$$

The $(\ell_3, m) = (2, -2)$ harmonics are given by the complex conjugate of the $(\ell_3, m) = (2, 2)$ harmonics.

As discussed, for example in [43], for a fixed ℓ_n one can relate the tensor harmonics on given basis to those on a different basis by a simple linear transformation.¹³ For the case at hand, we can relate the scalar derived tensor harmonics in the basis (C12) to the harmonics in the other basis (C2) as follows:

$$\mathbb{S}_{ab}^{(\ell_3, m)}(\chi, \phi) = R_a^c R_b^d \sum_{\ell_2=0}^{\ell_3} A_{\ell_2}^m \mathbb{S}_{cd}^{(\ell_3, \ell_2)}(\theta_3, \theta_2), \quad (\text{C15})$$

where in this expression (χ, ϕ) should be understood as functions of (θ_3, θ_2) and R_a^b is a rotation matrix given by

$$R = \begin{pmatrix} -\frac{\sin(\theta_2) \cos(\theta_3)}{\sqrt{1-\sin^2(\theta_2) \sin^2(\theta_3)}} & -\frac{\cos(\theta_2)}{\sqrt{1-\sin^2(\theta_2) \sin^2(\theta_3)}} & 0 \\ \frac{\cos(\theta_2)}{\sqrt{1-\sin^2(\theta_2) \sin^2(\theta_3)}} & -\frac{\sin(\theta_2) \cos(\theta_3)}{\sqrt{1-\sin^2(\theta_2) \sin^2(\theta_3)}} & 0 \\ 0 & 0 & 1 \end{pmatrix}. \quad (\text{C16})$$

For the $\ell_3 = 2$ scalar derived tensor harmonics, we find that the transformation matrix $A_{\ell_2}^m$ is given by:

$$A = \begin{pmatrix} \frac{1}{\sqrt{3}} & 0 & \sqrt{\frac{2}{3}} \\ -\frac{1}{\sqrt{3}} & \frac{i}{\sqrt{2}} & \frac{1}{\sqrt{6}} \\ -\frac{1}{\sqrt{3}} & -\frac{i}{\sqrt{2}} & \frac{1}{\sqrt{6}} \end{pmatrix}, \quad (\text{C17})$$

where the rows correspond to the values of $m = 0, 2, -2$ respectively, and similarly the columns correspond to the values of $\ell_2 = 0, 1, 2$. Furthermore, as shown in [43] reviewed in Appendix §E, the inverse of this matrix (C17), determines the transformation of the coefficients in the multipolar expansion of the Weyl scalars in different bases.

Appendix D: Tensor harmonics on the S^4

In this Appendix we collect some properties of tensor harmonics in S^4 . Furthermore, we list the harmonics that we have used to produce the waveforms in the main text.

1. Standard basis

We first write the metric on the S^4 in the standard form:

$$ds^2 = d\theta_4^2 + \sin^2 \theta_4 ds_{S^3}^2, \quad (\text{D1})$$

where $ds_{S^3}^2$ is the metric on the S^3 written as in (C1) and $\theta_4 \in [0, \pi]$. Furthermore, we choose the obvious basis of unit vectors on the S^4 :

$$\begin{aligned} m_{(1)} &= \frac{\partial}{\partial \theta_4}, \quad m_{(2)} = \frac{1}{\sin \theta_4} \frac{\partial}{\partial \theta_3}, \quad m_{(3)} = \frac{1}{\sin \theta_4 \sin \theta_3} \frac{\partial}{\partial \theta_2}, \\ m_{(4)} &= \frac{1}{\sin \theta_4 \sin \theta_3 \sin \theta_2} \frac{\partial}{\partial \theta_1}. \end{aligned} \quad (\text{D2})$$

The advantage of using this form of the metric on the S^4 is that we can easily construct tensor harmonics of any rank following the algorithm of [42]. To do so, we start from scalar harmonics on the S^4 . Since we are interested in spacetimes that possess an $\text{SO}(3)$ in $6D$, we can restrict ourselves to scalar harmonics that are constant on the S^2 sitting inside the S^3 , that in turn sits inside the S^4 , (D1). These (normalized) scalar harmonics are given by:

$$\mathbb{Y}^{(\ell_4, \ell_3)} = \frac{1}{\sqrt{4\pi}} c^{\ell_4, \ell_3} P_{\ell_4+1}^{-(\ell_3+1)}(\cos \theta_4) P_{\ell_3+1/2}^{-1/2}(\cos \theta_3), \quad (\text{D3})$$

where $P_\ell^m(x)$ are the associated Legendre polynomials,

$$c^{\ell_4, \ell_3} = (\ell_3 + 1) \sqrt{\frac{2\ell_4 + 3}{2} \frac{(\ell_4 + \ell_3 + 2)!}{(\ell_4 - \ell_3)!}}, \quad (\text{D4})$$

is the normalization constant, and $\ell_4 \geq \ell_3 \geq 0$. In this basis, the projected components of the tensor harmonics with $\ell_2 = \ell_1 = 0$ are:¹⁴

¹³ From representation theory, it follows that harmonics with different ℓ_n do not mix. Likewise, scalar derived tensor harmonics in one basis will only mix with the scalar derived tensor harmonics in the other basis.

¹⁴ Note that for this particular class of harmonics, $\mathbb{Y}_{44}^{(\ell_4, \ell_3)} = \mathbb{Y}_{33}^{(\ell_4, \ell_3)}$, where here \mathbb{Y} denotes any tensor harmonic.

a. *Scalar derived tensor harmonics*

- $(\ell_4, \ell_3) = (2, 0)$:

$$\begin{aligned}\mathbb{S}_{11}^{(2,0)} &= \frac{\sqrt{105}}{16\pi} \sin^2(\theta_4), \\ \mathbb{S}_{22}^{(2,0)} &= -\frac{1}{16\pi} \sqrt{\frac{35}{3}} \sin^2(\theta_4), \\ \mathbb{S}_{33}^{(2,0)} &= -\frac{1}{16\pi} \sqrt{\frac{35}{3}} \sin^2(\theta_4).\end{aligned}\quad (\text{D5})$$

- $(\ell_4, \ell_3) = (2, 1)$:

$$\begin{aligned}\mathbb{S}_{11}^{(2,1)} &= -\frac{1}{8\pi} \sqrt{\frac{21}{2}} \cos(\theta_3) \sin(2\theta_4), \\ \mathbb{S}_{12}^{(2,1)} &= \frac{1}{2\pi} \sqrt{\frac{7}{6}} \sin(\theta_3) \sin(\theta_4), \\ \mathbb{S}_{22}^{(2,1)} &= \frac{1}{8\pi} \sqrt{\frac{7}{6}} \cos(\theta_3) \sin(2\theta_4), \\ \mathbb{S}_{33}^{(2,1)} &= \frac{1}{8\pi} \sqrt{\frac{7}{6}} \cos(\theta_3) \sin(2\theta_4).\end{aligned}\quad (\text{D6})$$

- $(\ell_4, \ell_3) = (2, 2)$:

$$\begin{aligned}\mathbb{S}_{11}^{(2,2)} &= \frac{\sqrt{7}}{96\pi} [2 \cos(2\theta_3) + 1] [3 \cos(2\theta_4) + 5], \\ \mathbb{S}_{12}^{(2,2)} &= -\frac{\sqrt{7}}{6\pi} \sin(2\theta_3) \cos(\theta_4), \\ \mathbb{S}_{22}^{(2,2)} &= -\frac{\sqrt{7}}{96\pi} [2 \cos(2\theta_3) (\cos(2\theta_4) + 7) + \cos(2\theta_4) - 9], \\ \mathbb{S}_{33}^{(2,2)} &= -\frac{\sqrt{7}}{96\pi} [-4 \cos(2\theta_3) \sin^2(\theta_4) + \cos(2\theta_4) + 7].\end{aligned}\quad (\text{D7})$$

- $(\ell_4, \ell_3) = (4, 0)$:

$$\begin{aligned}\mathbb{S}_{11}^{(4,0)} &= \frac{\sqrt{1155}}{128\pi} \sin^2(\theta_4) [9 \cos(2\theta_4) + 7], \\ \mathbb{S}_{12}^{(4,0)} &= -\frac{1}{128\pi} \sqrt{\frac{385}{3}} \sin^2(\theta_4) [9 \cos(2\theta_4) + 7], \\ \mathbb{S}_{22}^{(4,0)} &= -\frac{1}{128\pi} \sqrt{\frac{385}{3}} \sin^2(\theta_4) [9 \cos(2\theta_4) + 7], \\ \mathbb{S}_{33}^{(4,0)} &= -\frac{1}{128\pi} \sqrt{\frac{385}{3}} \sin^2(\theta_4) [9 \cos(2\theta_4) + 7].\end{aligned}\quad (\text{D8})$$

- $(\ell_4, \ell_3) = (4, 1)$:

$$\begin{aligned}\mathbb{S}_{11}^{(4,1)} &= \frac{\sqrt{165}}{128\pi} \cos(\theta_3) [2 \sin(2\theta_4) - 9 \sin(4\theta_4)], \\ \mathbb{S}_{12}^{(4,1)} &= \frac{1}{32\pi} \sqrt{\frac{55}{3}} \sin(\theta_3) \sin(\theta_4) [9 \cos(2\theta_4) + 7], \\ \mathbb{S}_{22}^{(4,1)} &= \frac{1}{64\pi} \sqrt{\frac{55}{3}} \cos(\theta_3) \sin(\theta_4) [7 \cos(\theta_4) + 9 \cos(3\theta_4)], \\ \mathbb{S}_{33}^{(4,1)} &= \frac{1}{64\pi} \sqrt{\frac{55}{3}} \cos(\theta_3) \sin(\theta_4) [7 \cos(\theta_4) + 9 \cos(3\theta_4)].\end{aligned}\quad (\text{D9})$$

- $(\ell_4, \ell_3) = (4, 2)$:

$$\begin{aligned}\mathbb{S}_{11}^{(4,2)} &= \frac{1}{1536\pi} \sqrt{\frac{55}{2}} [2 \cos(2\theta_3) + 1] \\ &\quad \times [12 \cos(2\theta_4) + 81 \cos(4\theta_4) + 35], \\ \mathbb{S}_{12}^{(4,2)} &= -\frac{1}{192\pi} \sqrt{\frac{55}{2}} \sin(2\theta_3) [5 \cos(\theta_4) + 27 \cos(3\theta_4)], \\ \mathbb{S}_{22}^{(4,2)} &= \frac{1}{1536\pi} \sqrt{\frac{55}{2}} \{92 \cos(2\theta_4) - 27 \cos(4\theta_4) + 63 \\ &\quad - 2 \cos(2\theta_3) [52 \cos(2\theta_4) + 27 \cos(4\theta_4) + 49]\}, \\ \mathbb{S}_{33}^{(4,2)} &= -\frac{\sqrt{\frac{55}{2}}}{1536\pi} \{52 \cos(2\theta_4) + 27 \cos(4\theta_4) + 49 \\ &\quad - 8 \cos(2\theta_3) \sin^2(\theta_4) [27 \cos(2\theta_4) + 17]\}.\end{aligned}\quad (\text{D10})$$

- $(\ell_4, \ell_3) = (4, 3)$:

$$\begin{aligned}\mathbb{S}_{11}^{(4,3)} &= \frac{3\sqrt{55}}{256\pi} [\cos(\theta_3) + \cos(3\theta_3)] [2 \sin(2\theta_4) + 3 \sin(4\theta_4)], \\ \mathbb{S}_{12}^{(4,3)} &= -\frac{\sqrt{55}}{64\pi} [\sin(\theta_3) + 3 \sin(3\theta_3)] \sin(\theta_4) [3 \cos(2\theta_4) + 1], \\ \mathbb{S}_{22}^{(4,3)} &= \frac{\sqrt{55}}{64\pi} \cos(\theta_3) \sin(2\theta_4) \{8 - 3 \cos(2\theta_3) [\cos(2\theta_4) + 3]\}, \\ \mathbb{S}_{33}^{(4,3)} &= \frac{\sqrt{55}}{32\pi} \cos(\theta_3) \sin(2\theta_4) [3 \cos(2\theta_3) \sin^2(\theta_4) - 2].\end{aligned}\quad (\text{D11})$$

- $(\ell_4, \ell_3) = (4, 4)$:

$$\begin{aligned}\mathbb{S}_{11}^{(4,4)} &= \frac{3}{128\pi} \sqrt{\frac{11}{2}} \sin^2(\theta_4) [3 \cos(2\theta_4) + 5] \\ &\quad \times [2 \cos(2\theta_3) + 2 \cos(4\theta_3) + 1], \\ \mathbb{S}_{12}^{(4,4)} &= -\frac{3\sqrt{\frac{11}{2}}}{16\pi} \sin^2(\theta_4) \cos(\theta_4) [\sin(2\theta_3) + 2 \sin(4\theta_3)], \\ \mathbb{S}_{22}^{(4,4)} &= \frac{1}{64\pi} \sqrt{\frac{11}{2}} \sin^2(\theta_4) \{-3 \cos(4\theta_3) [\cos(2\theta_4) + 7] \\ &\quad + [6 \cos(2\theta_3) + 7] \sin^2(\theta_4) + 4 \cos^2(\theta_4)\}, \\ \mathbb{S}_{33}^{(4,4)} &= -\frac{1}{128\pi} \sqrt{\frac{11}{2}} \sin^2(\theta_4) \{6 \cos(2\theta_3) [\cos(2\theta_4) + 3] \\ &\quad - 12 \cos(4\theta_3) \sin^2(\theta_4) + 3 \cos(2\theta_4) + 13\}.\end{aligned}\quad (\text{D12})$$

b. *Vector derived tensor harmonics* There are three families of vector derived tensor harmonics on the S^4 but with our symmetry assumptions only one of them has a non-zero overlap with the Weyl scalars. The relevant vector harmonics for us are given by:

- $(\ell_4, \ell_3) = (2, 1)$

$$\begin{aligned}
\mathbb{V}_{11}^{(2,1)} &= -\frac{1}{8\pi} \sqrt{\frac{35}{2}} \sin(2\theta_4), \\
\mathbb{V}_{12}^{(2,1)} &= \frac{1}{12\pi} \sqrt{\frac{35}{2}} \sin(\theta_3) \sin(2\theta_4), \\
\mathbb{V}_{22}^{(2,1)} &= \frac{1}{24\pi} \sqrt{\frac{35}{2}} \sin(2\theta_4), \\
\mathbb{V}_{33}^{(2,1)} &= \frac{1}{24\pi} \sqrt{\frac{35}{2}} \sin(2\theta_4).
\end{aligned} \tag{D13}$$

- $(\ell_4, \ell_3) = (2, 2)$

$$\begin{aligned}
\mathbb{V}_{11}^{(2,2)} &= \frac{1}{12\pi} \sqrt{\frac{35}{2}} [2 \cos(2\theta_3) + 1] \cos(\theta_4), \\
\mathbb{V}_{12}^{(2,2)} &= -\frac{1}{24\pi} \sqrt{\frac{35}{2}} \sin(2\theta_3) [\cos(2\theta_4) + 3], \\
\mathbb{V}_{22}^{(2,2)} &= \frac{1}{12\pi} \sqrt{\frac{35}{2}} [1 - 2 \cos(2\theta_3)] \cos(\theta_4), \\
\mathbb{V}_{33}^{(2,2)} &= -\frac{1}{12\pi} \sqrt{\frac{35}{2}} \cos(\theta_4).
\end{aligned} \tag{D14}$$

- $(\ell_4, \ell_3) = (4, 1)$

$$\begin{aligned}
\mathbb{V}_{11}^{(4,1)} &= -\frac{\sqrt{77}}{32\pi} \cos(\theta_3) \sin(\theta_4) [9 \cos(2\theta_4) + 7], \\
\mathbb{V}_{12}^{(4,1)} &= \frac{\sqrt{77}}{192\pi} \sin(\theta_3) \sin(\theta_4) [37 \cos(\theta_4) + 27 \cos(3\theta_4)], \\
\mathbb{V}_{22}^{(4,1)} &= \frac{\sqrt{77}}{96\pi} \cos(\theta_3) \sin(\theta_4) [9 \cos(2\theta_4) + 7], \\
\mathbb{V}_{33}^{(4,1)} &= \frac{\sqrt{77}}{96\pi} \cos(\theta_3) \sin(\theta_4) [9 \cos(2\theta_4) + 7].
\end{aligned} \tag{D15}$$

- $(\ell_4, \ell_3) = (4, 2)$

$$\begin{aligned}
\mathbb{V}_{11}^{(4,2)} &= \frac{\sqrt{77}}{384\pi} [2 \cos(2\theta_3) + 1] [5 \cos(\theta_4) + 27 \cos(3\theta_4)], \\
\mathbb{V}_{12}^{(4,2)} &= -\frac{\sqrt{77}}{1536\pi} \sin(2\theta_3) [100 \cos(2\theta_4) + 81 \cos(4\theta_4) + 75], \\
\mathbb{V}_{22}^{(4,2)} &= \frac{\sqrt{77}}{384\pi} \{ [23 - 28 \cos(2\theta_3)] \cos(\theta_4) \\
&\quad + 9[1 - 4 \cos(2\theta_3)] \cos(3\theta_4) \}, \\
\mathbb{V}_{33}^{(4,2)} &= \frac{\sqrt{77}}{192\pi} \{ \cos(\theta_4) [18 \cos(2\theta_3) \sin^2(\theta_4) - 7] \\
&\quad - 9 \cos(3\theta_4) \}.
\end{aligned} \tag{D16}$$

- $(\ell_4, \ell_3) = (4, 3)$

$$\begin{aligned}
\mathbb{V}_{11}^{(4,3)} &= \frac{\sqrt{1155}}{64\pi} [\cos(\theta_3) + \cos(3\theta_3)] \sin(\theta_4) [3 \cos(2\theta_4) + 1], \\
\mathbb{V}_{12}^{(4,3)} &= -\frac{1}{64\pi} \sqrt{\frac{77}{15}} \sin(\theta_3) [3 \cos(2\theta_3) + 2] \\
&\quad \times \sin(\theta_4) [31 \cos(\theta_4) + 9 \cos(3\theta_4)], \\
\mathbb{V}_{22}^{(4,3)} &= \frac{1}{128\pi} \sqrt{\frac{77}{15}} \{ \cos(\theta_3) [13 \sin(\theta_4) + 9 \sin(3\theta_4)] \\
&\quad - 3 \cos(3\theta_3) [\sin(\theta_4) + 13 \sin(3\theta_4)] \}, \\
\mathbb{V}_{33}^{(4,3)} &= \frac{1}{64\pi} \sqrt{\frac{77}{15}} \cos(\theta_3) \{ [9 \cos(2\theta_3) - 4] \sin(\theta_4) \\
&\quad - 3[\cos(2\theta_3) + 4] \sin(3\theta_4) \}.
\end{aligned} \tag{D17}$$

- $(\ell_4, \ell_3) = (4, 4)$

$$\begin{aligned}
\mathbb{V}_{11}^{(4,4)} &= \frac{3}{32\pi} \sqrt{\frac{231}{5}} \sin^2(\theta_4) \cos(\theta_4) \\
&\quad \times [2 \cos(2\theta_3) + 2 \cos(4\theta_3) + 1], \\
\mathbb{V}_{12}^{(4,4)} &= -\frac{3}{64\pi} \sqrt{\frac{231}{5}} \sin(\theta_3) \sin^2(\theta_4) [\cos(2\theta_4) + 3] \\
&\quad \times [3 \cos(\theta_3) + 2 \cos(3\theta_3)], \\
\mathbb{V}_{22}^{(4,4)} &= \frac{1}{32\pi} \sqrt{\frac{231}{5}} [1 - 6 \cos(4\theta_3)] \sin^2(\theta_4) \cos(\theta_4), \\
\mathbb{V}_{33}^{(4,4)} &= -\frac{1}{32\pi} \sqrt{\frac{231}{5}} [3 \cos(2\theta_3) + 2] \sin^2(\theta_4) \cos(\theta_4).
\end{aligned} \tag{D18}$$

c. Transverse traceless tensor harmonics Given the symmetries of the spacetimes that we are considering, there is only one family of transverse traceless tensor harmonics on the S^4 that can contribute to the multipolar expansion of the Weyl scalars. The relevant tensor harmonics are given by:

- $(\ell_4, \ell_3) = (2, 2)$

$$\begin{aligned}
\mathbb{T}_{11}^{(2,2)} &= \frac{1}{12\pi} \sqrt{\frac{35}{2}} [2 \cos(2\theta_3) + 1], \\
\mathbb{T}_{12}^{(2,2)} &= -\frac{1}{6\pi} \sqrt{\frac{35}{2}} \sin(2\theta_3) \cos(\theta_4), \\
\mathbb{T}_{22}^{(2,2)} &= \frac{1}{12\pi} \sqrt{\frac{35}{2}} [4 \sin^2(\theta_3) \cos^2(\theta_4) - 1], \\
\mathbb{T}_{33}^{(2,2)} &= -\frac{1}{12\pi} \sqrt{\frac{35}{2}} [\sin^2(\theta_3) \cos(2\theta_4) + \cos^2(\theta_3)].
\end{aligned} \tag{D19}$$

- $(\ell_4, \ell_3) = (4, 2)$

$$\begin{aligned}\mathbb{T}_{11}^{(4,2)} &= \frac{1}{96\pi} \sqrt{\frac{55}{2}} [2 \cos(2\theta_3) + 1] [9 \cos(2\theta_4) + 7], \\ \mathbb{T}_{12}^{(4,2)} &= -\frac{1}{96\pi} \sqrt{\frac{55}{2}} \sin(2\theta_3) \cos(\theta_4) [27 \cos(2\theta_4) + 5], \\ \mathbb{T}_{22}^{(4,2)} &= \frac{1}{384\pi} \sqrt{\frac{11}{10}} \{4[26 - 71 \cos(2\theta_3)] \cos(2\theta_4) \\ &\quad + 378 \sin^2(\theta_3) \cos(4\theta_4) - 167 \cos(2\theta_3) + 27\}, \\ \mathbb{T}_{33}^{(4,2)} &= -\frac{1}{768\pi} \sqrt{\frac{11}{10}} \{ \cos(2\theta_3) [76 \cos(2\theta_4) + 113] \\ &\quad + 378 \sin^2(\theta_3) \cos(4\theta_4) + 284 \cos(2\theta_4) + 167\}.\end{aligned}\tag{D20}$$

- $(\ell_4, \ell_3) = (4, 3)$

$$\begin{aligned}\mathbb{T}_{11}^{(4,3)} &= \frac{3}{16\pi} \sqrt{\frac{55}{2}} [\cos(\theta_3) + \cos(3\theta_3)] \sin(2\theta_4), \\ \mathbb{T}_{12}^{(4,3)} &= -\frac{1}{4\pi} \sqrt{\frac{11}{10}} \sin(\theta_3) \sin(\theta_4) \\ &\quad \times [3 \cos(2\theta_3) + 2] [3 \cos(2\theta_4) + 2], \\ \mathbb{T}_{22}^{(4,3)} &= \frac{1}{16\pi} \sqrt{\frac{11}{10}} \cos(\theta_3) \\ &\quad \times \{21 \sin^2(\theta_3) \sin(4\theta_4) - [9 \cos(2\theta_3) + 1] \sin(2\theta_4)\}, \\ \mathbb{T}_{33}^{(4,3)} &= \frac{1}{32\pi} \sqrt{\frac{11}{10}} \cos(\theta_3) \\ &\quad \times \{[1 - 21 \cos(2\theta_3)] \sin(2\theta_4) - 21 \sin^2(\theta_3) \sin(4\theta_4)\}.\end{aligned}\tag{D21}$$

- $(\ell_4, \ell_3) = (4, 4)$

$$\begin{aligned}\mathbb{T}_{11}^{(4,4)} &= \frac{3}{16\pi} \sqrt{\frac{77}{10}} \sin^2(\theta_4) [2 \cos(2\theta_3) + 2 \cos(4\theta_3) + 1], \\ \mathbb{T}_{12}^{(4,4)} &= -\frac{3}{8\pi} \sqrt{\frac{77}{10}} \sin(\theta_3) \sin^2(\theta_4) \cos(\theta_4) \\ &\quad \times [3 \cos(\theta_3) + 2 \cos(3\theta_3)], \\ \mathbb{T}_{22}^{(4,4)} &= -\frac{1}{16\pi} \sqrt{\frac{77}{10}} \sin^2(\theta_4) \\ &\quad \times \{-3 \cos^2(\theta_3) [9 \cos(2\theta_4) + 7] \\ &\quad + 48 \cos^4(\theta_3) \cos^2(\theta_4) + 3 \cos(2\theta_4) + 2\}, \\ \mathbb{T}_{33}^{(4,4)} &= \frac{1}{256\pi} \sqrt{\frac{77}{10}} \{4[3 \cos(2\theta_3) + 6 \cos(4\theta_3) + 1] \cos(2\theta_4) \\ &\quad + 6 \sin^2(\theta_3) [4 \cos(2\theta_3) + 3] \cos(4\theta_4) \\ &\quad - 15 \cos(2\theta_3) - 18 \cos(4\theta_3) - 7\}.\end{aligned}\tag{D22}$$

2. Multipolar expansion of the Weyl scalars in the standard basis

The main advantage of using the standard form of the metric on the S^4 (D1) and the associated basis of vectors to ob-

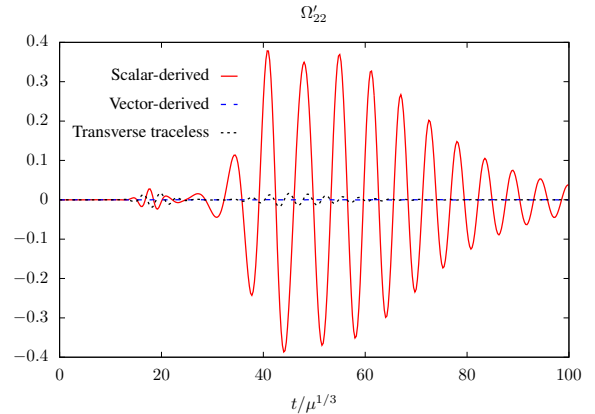


FIG. 8. Scalar derived, vector derived and transverse traceless tensor projections with $(\ell_4, \ell_3) = (2, 2)$ of the Weyl scalars for the same $a/\mu^{1/3} = 1.3$ run as in the main text. This figure illustrates that most of the signal is in the scalar derived sector. The same happens in any of the other simulations that we have performed.

tain the multipolar expansion of the Weyl tensor, is that one can systematically construct the required tensor harmonics of any rank. In this way, we can identify the sector of tensor harmonics captures most of the signal.

In Fig. 8 we display the $(\ell_4, \ell_3) = (2, 2)$ multipole of the Weyl scalars in the scalar derived, vector derived and transverse traceless tensor harmonics sectors for the same $a/\mu^{1/3} = 1.3$ simulation reported in the main text, Fig. 2. As this figure illustrates, most the signal is in the scalar derived sector. We have checked that this is the case in all our simulations and this is why in the main text we only report on the multipoles from the scalar derived tensor harmonics. Perhaps it should not be surprising that, given the symmetries of the spacetimes that we are considering, most the waveforms are captured by the scalar derived tensor harmonics.

The drawback of using the basis (D1) is that it is not aligned with the axis of rotation of the black hole spacetimes that we have considered. This has the consequence that the various harmonics with the same ℓ_4 but different ℓ_3 mix and one cannot accurately extract the frequencies and growth/decay rates of the various modes.¹⁵ This mixing of modes with the same ℓ_3 and different ℓ_2 's can be seen in Fig. 9. In this plot we display the $(\ell_4, \ell_3) = (2, 0)$, $(2, 1)$ and $(2, 2)$ multipoles of the Weyl scalars for the same $a/\mu^{1/3} = 1.3$ run as in the main text. As this plot suggests, the various modes appear to have similar frequencies and decay rates. To disentangle the various modes one would have to rotate the basis or consider an adapted basis. We chose the latter option.

¹⁵ This phenomenon was observed in [43] in 4D, for instance, when extracting gravitational waves from head on collisions of black holes and considering an extraction frame that is not suitably aligned with the collision axis. We would like to thank Ulrich Sperhake for pointing this out to us.

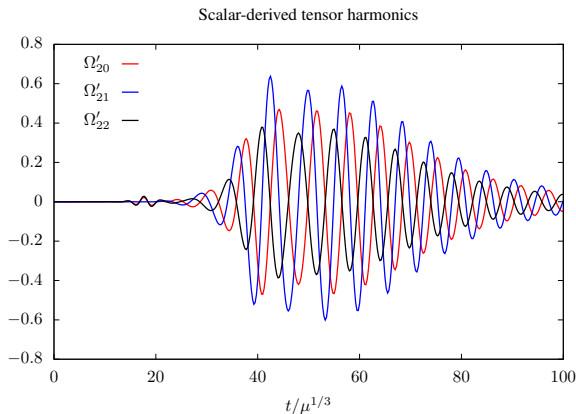


FIG. 9. Scalar derived tensor multipoles with $(\ell_4, \ell_3) = (2, 0)$, $(2, 1)$ and $(2, 2)$ of the Weyl scalars for the same $a/\mu^{1/3} = 1.3$ run as in the main text. This figure shows the mixing of modes with the same ℓ_4 and different ℓ_3 due to the misalignment between the chosen basis of angular vectors on the S^4 and the rotation axis of the black hole.

3. Adapted basis

As in the $5D$ case, it turns out to be convenient to write the metric on the S^4 in a form that makes the symmetries and the rotation plane of spacetimes that we consider manifest:

$$ds^2 = d\chi^2 + \sin^2 \chi d\phi^2 + \cos^2 \chi (d\theta^2 + \sin^2 \theta d\psi^2), \quad (\text{D23})$$

with $\chi \in [0, \pi/2]$, $\theta \in [0, \pi]$ and $\phi, \psi \in [0, 2\pi]$. In these coordinates, the angle ϕ on the extraction S^4 coincides with the angle on the rotation plane of the full spacetime. We choose the obvious basis of angular vectors on the S^4 written as in (D23):

$$m_{(1)} = \frac{\partial}{\partial \chi}, \quad m_{(2)} = \frac{1}{\sin \chi} \frac{\partial}{\partial \phi}, \quad m_{(3)} = \frac{1}{\cos \chi} \frac{\partial}{\partial \theta}, \quad (\text{D24})$$

$$m_{(4)} = \frac{1}{\cos \chi \sin \theta} \frac{\partial}{\partial \psi}.$$

In the previous subsection §D2, we have shown that the leading waveforms are in the sector of scalar derived tensor harmonics. Therefore, to accurately extract the leading modes that govern the dynamics of the black holes that we are interested in, we only need to concentrate on this sector of tensor harmonics. Scalar harmonics on the S^4 in the coordinates (D23) can be written as [44]

$$\mathbb{Y}^{\ell_4, m, \ell_2, \bar{m}} = N (\sin \chi)^{|m|} (\cos \chi)^{\ell_2} e^{im\phi} \mathbb{Y}_{\ell_2}^{\bar{m}}(\theta, \psi) \quad (\text{D25})$$

$${}_2F_1\left(\ell_2 + |m| - k, k + \frac{3}{2}, \ell_2 + \frac{3}{2}; \cos^2 \chi\right)$$

where N is a normalization constant, $\mathbb{Y}_{\ell_2}^{\bar{m}}(\theta, \psi)$ are the standard spherical harmonics on the S^2 , ${}_2F_1$ is the ordinary hypergeometric function and k is a positive integer related to the eigenvalue ℓ_4 by

$$\ell_4 = 2k - (\ell_2 + |m|). \quad (\text{D26})$$

Since we are considering spacetimes with a manifest $\text{SO}(3)$ symmetry, we only need to consider harmonics with $\ell_2 = 0$ (and consequently $\bar{m} = 0$) and hence we will drop the corresponding labels from now on.

Writing the S^4 as in (D23) and in the basis (D24), the projected scalar derived tensor harmonics obtained from (D25) are:

- $(\ell_4, m) = (2, 0)$:

$$\mathbb{S}_{11}^{(2,0)} = \frac{1}{48\pi} \sqrt{\frac{35}{2}} [3 \cos(2\chi) + 1],$$

$$\mathbb{S}_{22}^{(2,0)} = -\frac{1}{48\pi} \sqrt{\frac{35}{2}} [\cos(2\chi) - 5], \quad (\text{D27})$$

$$\mathbb{S}_{33}^{(2,0)} = -\frac{1}{48\pi} \sqrt{\frac{35}{2}} [\cos(2\chi) + 3].$$

- $(\ell_4, m) = (2, 2)$:

$$\mathbb{S}_{11}^{(2,2)} = \frac{1}{32\pi} \sqrt{\frac{7}{3}} e^{2i\phi} [3 \cos(2\chi) + 5],$$

$$\mathbb{S}_{21}^{(2,2)} = \frac{i}{4\pi} \sqrt{\frac{7}{3}} e^{2i\phi} \cos(\chi), \quad (\text{D28})$$

$$\mathbb{S}_{22}^{(2,2)} = -\frac{1}{32\pi} \sqrt{\frac{7}{3}} e^{2i\phi} [\cos(2\chi) + 7],$$

$$\mathbb{S}_{33}^{(2,2)} = \frac{1}{16\pi} \sqrt{\frac{7}{3}} e^{2i\phi} \sin^2(\chi),$$

- $(\ell_4, m) = (4, 0)$:

$$\mathbb{S}_{11}^{(4,0)} = -\frac{\sqrt{77}}{1536\pi} [12 \cos(2\chi) + 81 \cos(4\chi) - 29],$$

$$\mathbb{S}_{22}^{(4,0)} = \frac{\sqrt{77}}{1536\pi} [-92 \cos(2\chi) + 27 \cos(4\chi) + 1], \quad (\text{D29})$$

$$\mathbb{S}_{33}^{(4,0)} = \frac{\sqrt{77}}{1536\pi} [52 \cos(2\chi) + 27 \cos(4\chi) - 15].$$

- $(\ell_4, m) = (4, 2)$:

$$\mathbb{S}_{11}^{(4,2)} = -\frac{1}{256\pi} \sqrt{\frac{55}{6}} e^{2i\phi} [12 \cos(2\chi) + 27 \cos(4\chi) - 7],$$

$$\mathbb{S}_{21}^{(4,2)} = \frac{i}{64\pi} \sqrt{\frac{55}{6}} e^{2i\phi} [\cos(\chi) - 9 \cos(3\chi)],$$

$$\mathbb{S}_{22}^{(4,2)} = \frac{1}{256\pi} \sqrt{\frac{55}{6}} e^{2i\phi} [4 \cos(2\chi) + 9 \cos(4\chi) + 19],$$

$$\mathbb{S}_{33}^{(4,2)} = -\frac{1}{64\pi} \sqrt{\frac{55}{6}} e^{2i\phi} \sin^2(\chi) [9 \cos(2\chi) + 11], \quad (\text{D30})$$

- $(\ell_4, m) = (4, 4)$:

$$\begin{aligned}
\mathbb{S}_{11}^{(4,4)} &= \frac{3}{128\pi} \sqrt{\frac{55}{2}} e^{4i\phi} \sin^2(\chi) [3 \cos(2\chi) + 5], \\
\mathbb{S}_{21}^{(4,4)} &= \frac{3i}{16\pi} \sqrt{\frac{55}{2}} e^{4i\phi} \sin^2(\chi) \cos(\chi), \\
\mathbb{S}_{22}^{(4,4)} &= -\frac{3}{128\pi} \sqrt{\frac{55}{2}} e^{4i\phi} \sin^2(\chi) [\cos(2\chi) + 7], \\
\mathbb{S}_{33}^{(4,4)} &= \frac{3}{64\pi} \sqrt{\frac{55}{2}} e^{4i\phi} \sin^4(\chi).
\end{aligned} \tag{D31}$$

The $(\ell_4, m) = (2, -2), (4, -2), (4, -4)$ harmonics are given by the complex conjugate of the $(2, 2), (4, 2), (4, 4)$ respectively.

As we have already seen in §C 2, for a fixed ℓ_4 we can relate the harmonics in this basis (D24) to those in the standard basis (D2) by a linear transformation,

$$\mathbb{S}_{ab}^{(\ell_4, m)}(\chi, \phi) = R_a^c R_b^d \sum_{\ell_3=0}^{\ell_4} A^m_{\ell_3} \mathbb{S}_{cd}^{(\ell_4, \ell_3)}(\theta_4, \theta_3), \tag{D32}$$

where in the l.h.s of this expression (χ, ϕ) should be understood as functions of (θ_4, θ_3) , and R_a^b is a rotation matrix given by

$$R = \begin{pmatrix} -\frac{\sin(\theta_3) \cos(\theta_4)}{\sqrt{1-\sin^2(\theta_3) \sin^2(\theta_4)}} & -\frac{\cos(\theta_3)}{\sqrt{1-\sin^2(\theta_3) \sin^2(\theta_4)}} & 0 & 0 \\ \frac{\cos(\theta_3)}{\sqrt{1-\sin^2(\theta_3) \sin^2(\theta_4)}} & -\frac{\sin(\theta_3) \cos(\theta_4)}{\sqrt{1-\sin^2(\theta_3) \sin^2(\theta_4)}} & 0 & 0 \\ 0 & 0 & 1 & 0 \\ 0 & 0 & 0 & 1 \end{pmatrix}. \tag{D33}$$

For the $\ell_4 = 2$ scalar derived tensor harmonics, the transformation matrix is given by

$$A^m_{\ell_3} = \begin{pmatrix} \frac{\sqrt{3}}{2\sqrt{2}} & 0 & \frac{\sqrt{5}}{2\sqrt{2}} \\ \frac{\sqrt{5}}{4} & \frac{i}{\sqrt{2}} & -\frac{\sqrt{3}}{4} \\ \frac{\sqrt{5}}{4} & -\frac{i}{\sqrt{2}} & -\frac{\sqrt{3}}{4} \end{pmatrix}, \tag{D34}$$

where the rows correspond to $m = 0, 2, -2$ and the columns correspond to $\ell_3 = 0, 1, 2$. Similarly, for the $\ell_4 = 4$ harmonics we find,

$$A^m_{\ell_3} = \begin{pmatrix} \frac{\sqrt{15}}{8} & 0 & \frac{\sqrt{35}}{8\sqrt{2}} & 0 & \frac{3}{8}\sqrt{\frac{7}{2}} \\ \frac{\sqrt{7}}{4\sqrt{2}} & \frac{i}{2\sqrt{2}} & \frac{\sqrt{3}}{8} & \frac{i}{2}\sqrt{\frac{3}{2}} & -\frac{\sqrt{15}}{8} \\ \frac{\sqrt{7}}{4\sqrt{2}} & -\frac{i}{2\sqrt{2}} & \frac{\sqrt{3}}{8} & -\frac{i}{2}\sqrt{\frac{3}{2}} & -\frac{\sqrt{15}}{8} \\ \frac{\sqrt{21}}{8\sqrt{2}} & \frac{i}{2}\sqrt{\frac{3}{2}} & -\frac{9}{16} & -\frac{i}{2\sqrt{2}} & \frac{\sqrt{5}}{16} \\ \frac{\sqrt{21}}{8\sqrt{2}} & -\frac{i}{2}\sqrt{\frac{3}{2}} & -\frac{9}{16} & \frac{i}{2\sqrt{2}} & \frac{\sqrt{5}}{16} \end{pmatrix}, \tag{D35}$$

where the rows correspond to $m = 0, 2, -2, 4, -4$ and the columns correspond to $\ell_3 = 0, 1, 2, 3, 4$ respectively.

Appendix E: Transformation of the Weyl multipoles under changes of basis

In this subsection we review the transformations of the Weyl multipoles under rotations of the basis vectors and relate them to the transformation properties of the tensor harmonics. This is a straightforward generalization of the results in [43] to the higher dimensions.

The expansion of the Weyl scalars in multipoles is given by

$$\Omega'_{AB}(\theta) = \sum_{\ell} \psi_{\ell} \mathbb{Y}_{AB}^{\ell}(\theta) \tag{E1}$$

where ℓ is a collective label that specifies each of the tensor harmonics on the S^n at infinity, θ denotes the collection of angles on such sphere and ψ_{ℓ} are the corresponding multipoles. Under a rotation, $\Omega'_{AB}(\theta)$ transforms as

$$\Omega'_{AB}(\theta') = R_A^C R_B^D \Omega'_{CD}(\theta(\theta')), \tag{E2}$$

where the R_A^B are rotation matrices. Given the transformation of the harmonics under rotations,

$$\mathbb{Y}_{AB}^{\ell'}(\theta') = R_A^C R_B^D \sum_{\ell} A^{\ell'}_{\ell} \mathbb{Y}_{AB}^{\ell}(\theta), \tag{E3}$$

it follows that

$$\psi_{\ell'} = \sum_{\ell} \psi_{\ell} (A^{-1})^{\ell}_{\ell'} \tag{E4}$$

This transformation rule allows us to compute the Weyl multipoles in the (D24) from the multipoles computed in the standard basis (D2).

Appendix F: Apparent horizon and contours of χ

In cases where the AH is a star-shaped surface, we find that contours of the conformal factor χ closely track the AH obtained by our apparent horizon finder. Fig. 10 demonstrates this for a 6D MP black hole of dimensionless spin $a/\mu^{1/3} = 1.3$ an initial $m = 2$ deformation in χ described by (4),(5). For this simulation, the AH can be tracked by our apparent horizon finder for the entire evolution. The AH at early times is roughly followed by the $\chi \sim 0.4$ contour, and as the gauge evolution proceeds, the AH at late times is most closely followed by the $\chi \sim 0.6$ contour. In particular, at time $t/\mu^{1/3} \sim 30$ when the AH is most elongated, the AH remains well-described by the $\chi \sim 0.6$ contour.

Following χ contours is particularly useful when the AH ceases to be star-shaped, and can no longer be tracked by our apparent horizon finder (though, see [14, 27] for different apparent horizon finder implementations that get around the star-shaped requirement). Fig. 11 and Fig. 12 show the χ contours for two such cases of 6D MP black holes of dimensionless spin $a/\mu^{1/(D-3)} = 1.5$ with initial $m = 2$ and $m = 4$ deformations in χ , respectively, along with their AH shapes for as long as they can be tracked.

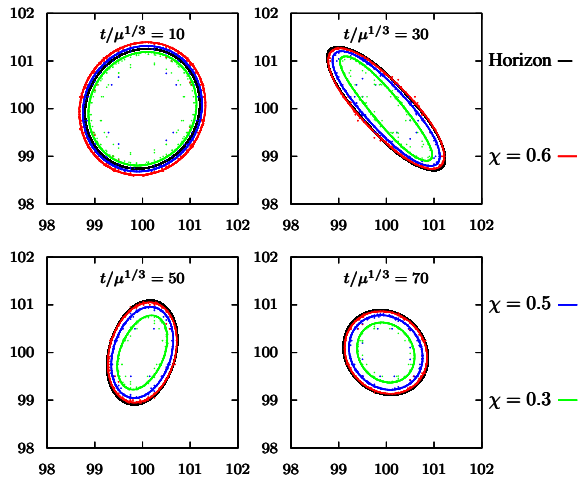


FIG. 10. Several χ contours for a 6D MP BH with $a/\mu^{1/3} = 1.3$ and an initial $m = 2$ deformation. The AH can be tracked throughout the evolution, and is well-described by the $\chi \sim 0.4$ contour at early times, and by the $\chi \sim 0.6$ contour at late times.

Fig. 11 corresponds to an initial $m = 2$ deformation, and Fig. 12 to an initial $m = 4$ deformation. In both cases, the AH at early times is roughly followed by the $\chi \sim 0.4$ contour, and the gauge appears to evolve in such a way that the AH at late times is well-described by the $\chi \sim 0.5$ contour. Thus, we continue to use the $\chi \sim 0.5$ contour as a proxy for the AH shape even at late times when the AH can no longer be found. With this proxy, the MP BH with an initial $m = 2$ deformation develops a thin bar shape (see the last panel of Fig. 11), and the MP BH with an initial $m = 4$ deformation develops four thin arms (see the last panel of Fig. 12).

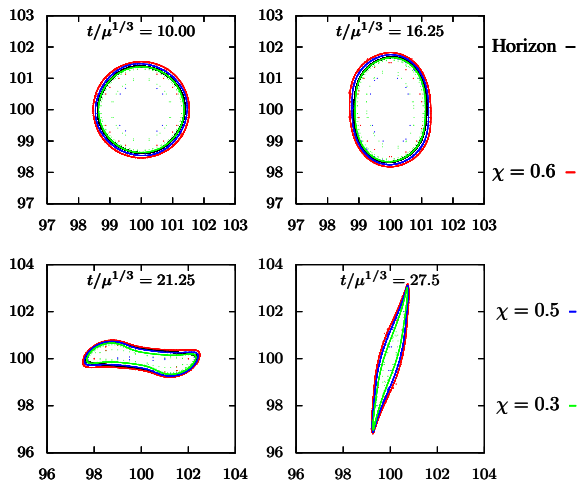


FIG. 11. Several χ contours for a 6D MP BH with $a/\mu^{1/3} = 1.5$ and an initial $m = 2$ deformation. The AH is well-described by the $\chi \sim 0.4$ contour at early times (see first two panels), and by $\chi \sim 0.5$ at the last time slice when the apparent horizon finder can still track the AH location (see third panel).

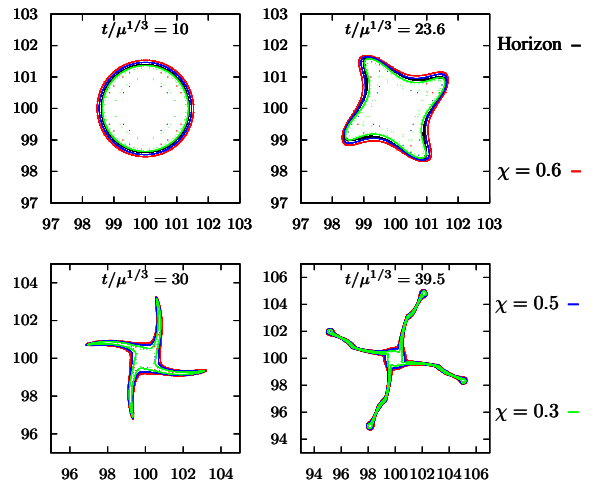


FIG. 12. Several χ contours for a 6D MP BH with $a/\mu^{1/3} = 1.5$ and an initial $m = 4$ deformation. The AH is well-described by the $\chi \sim 0.4$ contour at early times (see first panel), and by $\chi \sim 0.5$ at the last time slice when the apparent horizon finder can still track the AH location (see second panel).

Appendix G: Convergence Test

Here we present a numerical test taken from a simulation of a 6D MP BH perturbed at $t/\mu^{1/3} = 10$ by an $m = 2$ deformation in χ described by eqs. (4) and (5). We plot the resulting gravitational waveform via the h_+ component of the metric perturbation given by (10), extracted on the z -axis at $z/\mu^{1/3} = 29$. This is done at three different resolutions, where each linear dimension is covered by 80, 120, and 160 points, respectively. The point-wise difference in the waveform between subsequent resolutions yields a convergence factor of ~ 3 , which indicates a rate convergence that is between 2^{nd} and 3^{rd} order.

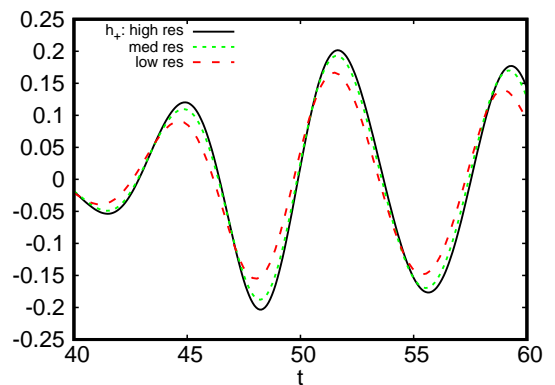


FIG. 13. Convergence test of the gravitational wave data from a 6D MP BH. Here, we have zoomed in on the time interval where the wave is most prominent. The coarsest grid of the low, medium, and high resolution simulations covers each linear dimension by 80, 120, and 160 points, respectively.